Sea Ice CCI+

ESA CCI+ CLIMATE CHANGE INITIATIVE
PHASE 1: NEW R&D ON CCI ECVS

Contract number:
4000126449/19/I-NB

CCI+ Sea Ice ECV

SEA ICE THICKNESS ALGORITHM THEORETICAL BASIS DOCUMENT (ATBD)

Reference: D2.1

Issue: 2.1

Date: 25 June 2020

Norwegian Meteorological Institute	**The Norwegian Meteorological Institute (METNO)** Henrik Mohns Plass 1 N-0313 Oslo Norway Phone: + 47 22 96 30 00 Fax: + 47 22 96 30 50 E-Mail: thomas.lavergne@met.no http://www.met.no

Contract	**Deliverable**
Phase 1 of the CCI+ Climate Change Initiative NEW R&D ON CCI ECVs Sea Ice ECV	D2.1 Sea Ice Thickness Algorithm Theoretical Basis Document
CLIENT	**CLIENT REFERENCE**
European Space Agency	4000126449/19/I-NB
Revision date:	**Approval date:**
25 June 2020	17 July 2020

Principal Authors

Heidi Sallila, Finnish Meteorological Institute

Eero Rinne, Finnish Meteorological Institute

Stefan Hendricks, Alfred Wegener Institute

Change Record

Issue	Date	Reason for Change	Author(s)
1.0	29 August 2019	First version	H. Sallila, E. Rinne, S. Hendricks
2.0	29 May 2020	Second version	H. Sallila, E. Rinne, S. Hendricks
2.1	25 June 2020	Response to the RID_D2.1_SIT_v2.0	H. Sallila, E. Rinne, S. Hendricks

Document Approval

Role	Name	Signature
Written by:	H. Sallila, E. Rinne, S. Hendricks	
Checked by:	M. A. Killie	
Approved by:	A. M. Trofaier	

Contents

0.1 List of Figures

0.2 List of Tables

1 INTRODUCTION

1.1 Purpose

This document is the Algorithm Theoretical Basis for the Sea Ice ECV within CCI+ PHASE 1 - NEW R&D ON CCI ECVs, which is being undertaken by a METNO-led consortium. This document is based on the work of phase 2 of the ESA CCI project and includes the new developments for the Sea Ice Thickness (SIT) aspects.

This document also contains preparation and documentation of the ongoing work to extend the CRDP to cover SIT from ERS-1 and ERS-2 satellites as well as for future level-4 products and computation of sea-ice volume. At the time of writing, these development items are not complete and these sections will be updated in the future versions of this document.

1.2 Scope

The scope of the document is to describe elements of the algorithms that are chosen for implementation during the first year of the CCI+ Phase 1, towards the first production of test products during Year 1. The selected algorithms are presented and justified, but the document does not contain the results of research leading to the selection of these algorithms.

1.3 Document Status

This is the second issue of the ATBD document for the Sea Ice CCI+ project. The document describes the algorithms used for the preliminary processing, which will go through further development in the future versions. In addition, the auxiliary data sets used in the initial processing are introduced.

The description of the SIT retrieval algorithm reflects the state at the end of the Phase 2 of the SICCI project, with the added knowledge gained from ERS-1 and ERS-2 studies, as well as the exception of novel snow estimates for the Arctic in areas where Warren climatology is considered outdated. This document will be iterated after the SIT algorithm development has progressed. This version of the document has undergone some structural changes from the previous version, in order to deliver a fluent description of the algorithm steps and to better conform the SIC ATBD.

1.4 Acronyms and Abbreviations

Table 1-1 below lists the acronyms and abbreviations used in this volume.

Table 1-1: Acronyms and Abbreviations. Acronyms for the deliverable items (URD, etc…) and partner institutions (AWI,..) are not repeated.

Acronym	Meaning
AMSR-E / AMSR2	Advanced Microwave Scanning Radiometer (for EOS / #2)

AOGCM	Arctic Ocean General Climate Model
AR5, AR6	WMO IPCC Assessment Report series
ASAR	Advanced Synthetic Aperture Radar
C3S	EU Copernicus Climate Change Service
CCI	Climate Change Initiative
CDR	Climate Data Record
CMEMS	EU Copernicus Marine Environment Monitoring Service
CMIP5, CMIP6	Coupled Model Intercomparison Project series
CMUG	Climate Modelling User Group
CRG	Climate Research Group
CS-2	ESA's CryoSat-2
DEWG	CCI Data Engineering Working Group
EASE grid	Equal-Area Scalable Earth Grid
ECMWF	European Centre for Medium-Range Weather Forecasts
ECV	Essential Climate Variable
ENVISAT	ESA's Environmental Satellite
EO	Earth Observation
ERS	European Remote Sensing Satellite
ESA	European Space Agency
ESMR	Electrically Scanning Microwave Radiometer
EUMETSAT	European Organization for the Exploitation of Meteorological Satellites
FoV (*alt* FOV)	Field-of-View
FY3	Feng Yun 3
FYI	First Year Ice
GCOS	WMO's Global Climate Observing System
GCW	WMO's Global Cryosphere Watch
ICDR	Interim Climate Data Record
IMB	Ice Mass Balance buoy
IPCC	WMO's Intergovernmental Panel on Climate Change
L1b, L2, L3C, ...	Satellite data processing Level (Level-1b, …)
MERIS	MEdium Resolution Imaging Spectrometer
EPS, EPS-SG	EUMETSAT's Polar System, EPS Second Generation
MIZ	Marginal Ice Zone
MODIS	Moderate Resolution Imaging Spectroradiometer
MWI	MicroWave Imager (EPS-SG)
MWRI	Micro-Wave Radiation Imager (Feng Yun 3)
MYI	Multi-Year Ice
NASA	National Aeronautics and Space Administration

NOAA	US National Oceanic and Atmospheric Administration
NSIDC	US National Snow and Ice Data Centre
OE	Optimal Estimation
OIB	Operation Ice Bridge
OSI SAF	EUMETSAT Ocean and Sea Ice Satellite Application Facility
OWF	Open Water Filter
PMR	Passive Microwave Radiometer
PMW	Passive Microwave
RA	Radar Altimeter
RRDP	Round Robin Data Package
SIC	Sea Ice Concentration
SIT	Sea Ice Thickness
SAR	Synthetic Aperture Radar
SGDR	Sensor Geophysical Data Record
SIRAL	Synthetic Aperture Radar (SAR) Interferometer Radar Altimeter
SOA	Service Oriented Architecture
SMMR	Scanning Multichannel Microwave Radiometer
SMOS	Soil Moisture and Ocean Salinity
SSM/I	Special Sensor Microwave/Imager
SSMIS	Special Sensor Microwave Imager/Sounder
ULS	Upward Looking Sonar
WMO	World Meteorological Organisation
WSM	Wide Swath Mode

1.5 Executive Summary

This document presents the algorithms for producing the Sea Ice Thickness Climate Data Record (SIT CDR) in CCI+. This document can be understood as a recipe book for a software engineer wanting to build a working SIT processor. It also gives the background of used algorithms and data for anyone wanting to understand the CRDP better.

The document includes all the necessary steps for converting altimeter waveforms into sea ice thickness in along-track (L2) as well as monthly gridded (L3) format and the gap-free gridded (L4):

- Filtering data based on latitudes, possibly removing data points based on flags provided with the data
- Surface-type classification algorithms based on waveform parameters for differentiating between ocean, lead, sea ice and ambiguous
- Waveform retracking of the difference surface types to obtain ice elevations and sea surface height tie points over leads between ice floes.

- Application of geophysical range corrections including tidal correction
- Estimation of radar freeboard and along-track sea surface height from ice surface elevations and interpolated SSH tie points utilizing a mean sea surface
- Radar freeboard to sea-ice freeboard conversion by applying geometric corrections, with snow information
- Sea ice thickness calculation based on sea-ice freeboard and auxiliary parameters and the assumptions of hydrostatic equilibrium

Along with steps and algorithms, all primary and auxiliary data products used to create the SIT CDR are introduced.

As the algorithms mature, the ATBD will be updated throughout the project. In particular, ERS-1 and ERS-2 algorithms will undergo changes in the future versions of this document.

2 INPUT AND AUXILIARY DATA

2.1 Overview

This part of the document is intended as a generic guide to setting up a sea ice thickness processing system for any polar orbiting satellite radar altimeter. The general method is described and specific examples are given. The general processing system is identical for pulse-limited as well as for SAR altimetry. Any sensor type specific differences are stated.

The method used to extract sea ice thickness from radar altimetry data is based on the pioneering work of Peacock and Laxon, 2004; Laxon et al., 2003 for the ERS-2 mission. The method involves separating the radar echoes returning from the ice floes from those returning from the sea surface in the leads between the floes. This step of a surface-type classification is crucial and allows for a separate determination of the ice floe and sea surface heights. The freeboard that is the elevation of the ice upper side (or ice-snow interface) above the sea level can then be computed by deducting the interpolated sea surface height at the floe location from the height of the floe. Sea-ice thickness can then be calculated from the sea-ice freeboard with the additional information of the snow load. Figure 2-1 shows an example of the earliest results of Laxon et al. (2003) with aggregated ERS data. Figure 2-2 and Figure 2-3 show the progression in terms of spatial and temporal resolution of altimeter-based sea ice thickness information with the extension to the Envisat and CryoSat-2 platforms in the ESA CCI project since the first application of the method.

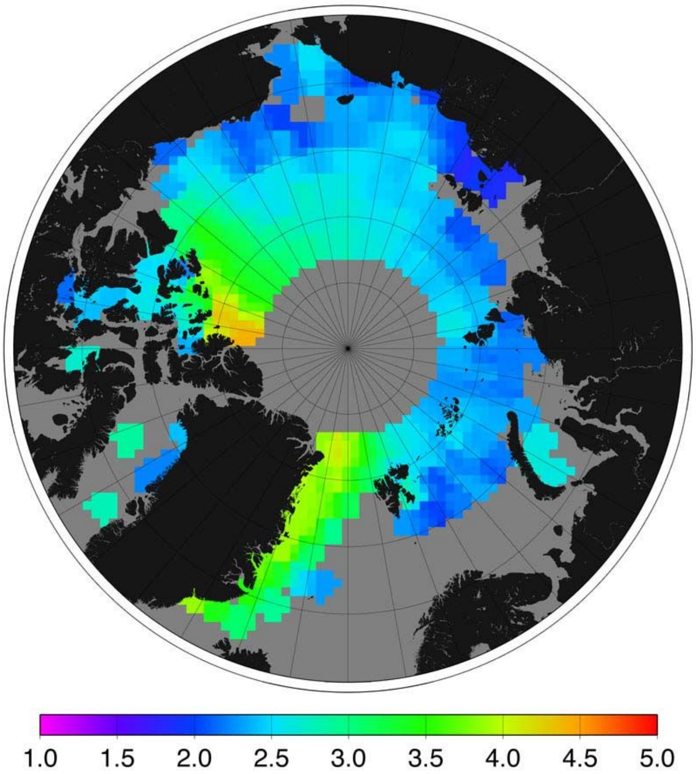

Figure 2‑1: Average winter (October to March) Arctic sea ice thickness in meters from October 1993 to March 2001 computed from pulse-limited ERS satellite altimeter measurements.

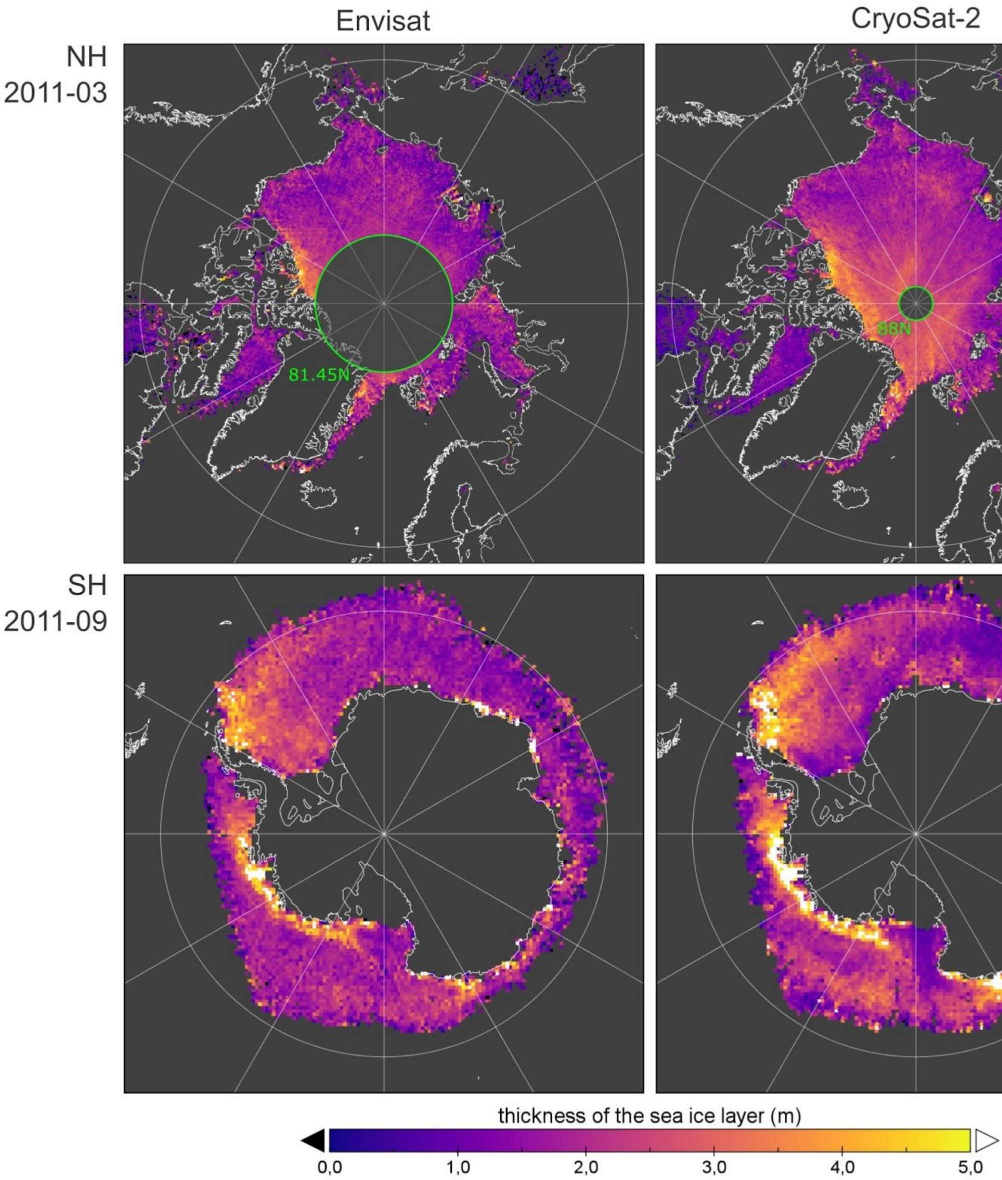

Figure 2‑2: Monthly gridded sea ice thickness data in the northern hemisphere with orbit coverage limits for March 2011 (top panel): Envisat (left) and CryoSat-2 (right) and in the southern hemisphere for September 2011 (lower panel)

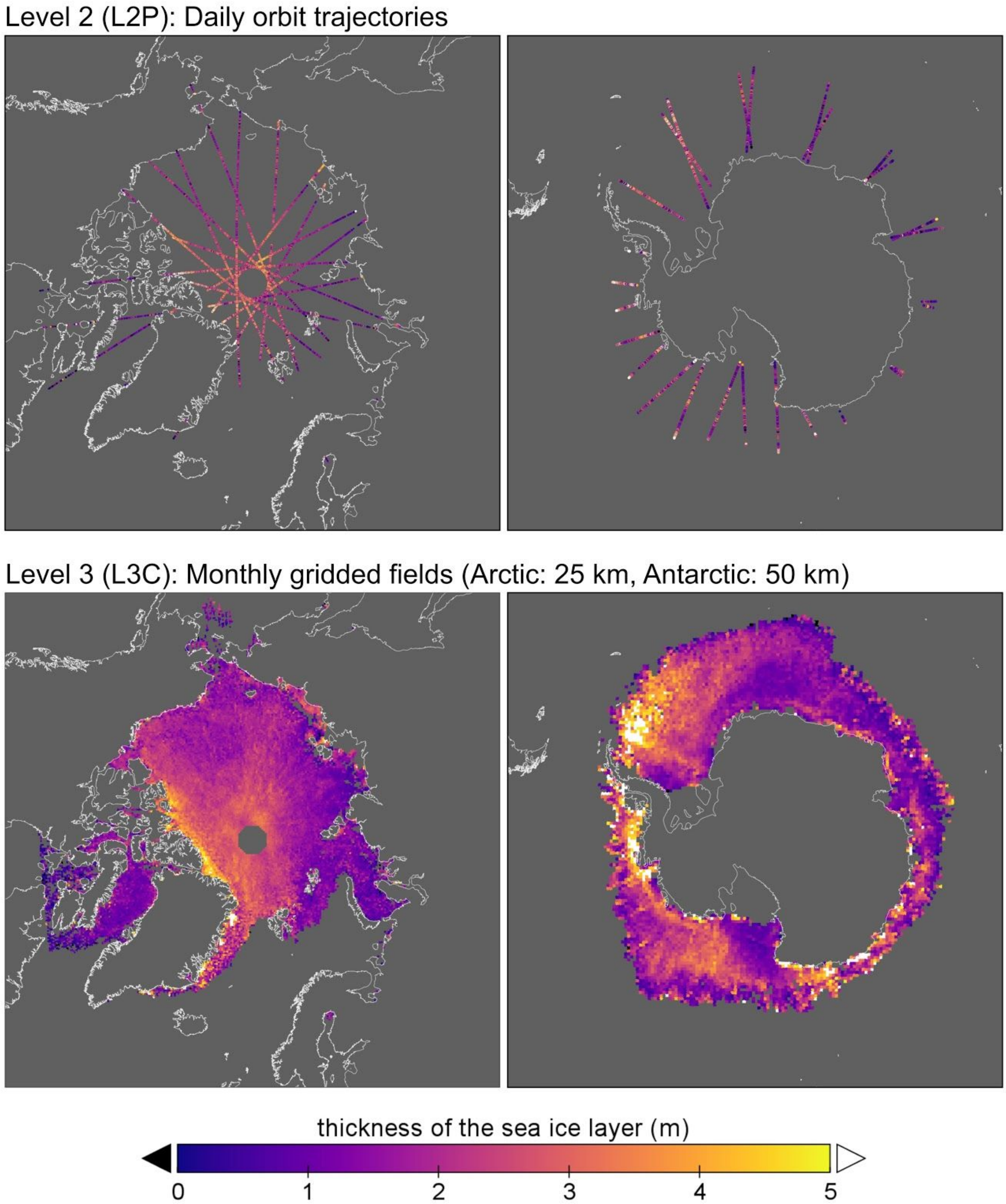

Figure 2‑3: Sea-ice thickness product level examples in both hemispheres. top: Daily orbit trajectories (l2p), bottom: monthly data on space-time grid with different resolution for northern and southern hemisphere.

2.2 Primary Altimeter Data Sets

The input data set must contain the radar echo waveforms and all other fields mentioned in this document such as altitude, range, atmospheric corrections and geophysical corrections. Figure 3-1 shows a flow chart for each step of the sea ice thickness processor. Each step is explained in detail in the sections below. For ERS-1 and ERS-2 RA the REAPER Sensor Geophysical Data Record (SGDR) data is used. In the case of Envisat RA-2, the input for the sea ice thickness processor is version 3.0 of the Envisat SGDR data. The SGDR data contains the waveforms as well as all other required fields. The ERS data is provided per cycle files or daily files. For Envisat data, each orbit is stored in two data files. The earlier of the two data files contains the data for the ascending arc from -81.5 latitude up to +81.5 latitude, and the later of the two the descending arc from +81.5 latitude back down to -81.5 latitude. These files are read sequentially and the output split at appropriate points to make continuous Arctic and Antarctic passes.

For CryoSat-2, the current version of Baseline C orbit data files are used and separated into sections of different instrument modes by the processor. The algorithm version Baseline D is generated by ESA at the time of this version of the document and the newer version will be used when available. CryoSat-2's SIRAL altimeter is operated in two different modes over sea ice: a) In synthetic aperture radar (SAR) off-coast and b) in synthetic aperture radar interferometric (SIN) mode to enable more accurate land ice altimeter measurements with higher surface slopes. For the product generation both radar modes are used, but the processing does not utilize the interferometric information in SIN mode. In addition to the different altimeter type that improves the spatial resolution, the higher orbit inclination of CryoSat-2 allows sea ice thickness measurements in the Arctic up to 88N.

2.3 Auxiliary data

The conversion into sea-ice freeboard requires either the use of auxiliary input data or a parametrization of snow depth. For the Arctic, where in SICCI Phase 2 only Warren climatology (W99, Warren et al., 1999) was applied, we now use a merged Warren-AMSR2 (W99-AMSR2) snow climatology for all the instruments, further described in Section 5.5. One main reason for the change is that the Warren climatology is based on data sets obtained from Arctic drift stations in regions of multi-year sea ice (MYI), snow depth values are suspected to be biased high over first-year sea-ice (FYI).

In order to discriminate between FYI and MYI in the Arctic, we resort to Copernicus Climate Change Service (C3S) Climate Data Record (CDR)/interim-CDR (ICDR). In SICCI Phase 2 a MYI fraction data set based on the Special Sensor Microwave Imager (SSM/I)/Special Sensor Microwave Imager Sounder (SSMIS) sensors on-board of the Defense Meteorological Satellite Program (DMSP) satellites provided by the Integrated Climate Data Center (ICDC) was used. The C3S CDR is produced with an algorithm that is optimized to produce consistent CDRs based on time series of passive microwave data of the above mentioned instruments, in addition with SMMR and ECMWF ERA-Interim data.

Table 2-1: Summary of used auxiliary data sets.

Parameter	ERS-1 /2 Arctic	ERS- 1 / 2 Antarctic	Envisat RA-2 Arctic	Envisat RA-2 Antarctic	CryoSat-2 Arctic	CryoSat-2 Antarctic
SIC	C3S CDR	C3S CDR	C3S CDR	C3S CDR	C3S CDR/ICDR	C3S CDR/ICDR
SIType	C3S CDR	Single Ice Type	C3S CDR	Single Ice Type	C3S CDR/ICDR	Single Ice Type
Snow	Merged	AMSR-e	Merged	AMSR-E/2	Merged	AMSR-E/2

Depth	W99-AMSR2 climatology	climatology	W99-AMSR2 climatology	climatology	W99-AMSR2 climatology	climatology
Snow Density	Warren99	fixed/clim	Warren99	fixed/clim	Warren99	fixed/clim
MSS	DTU18	DTU18	DTU18	DTU18	DTU18	DTU18

For the Antarctic, we assume only a single sea-ice type being present. As the Warren climatology is only available for the Arctic, we use a snow-depth climatology derived from the Advanced Microwave Scanning Radiometer-EOS (AMSR-E) and AMSR-2 data for the Antarctic. This data set is based on a revised version of the approach described by Cavalieri et al. (2014) and provided by the ICDC.

Other required auxiliary input data sets for the estimation of sea ice freeboard and sea ice thicknesses comprise the use the sea-ice concentration (SIC) data obtained from the C3S CDR for both hemispheres, in contrast to the SIC product from Ocean and Sea Ice Satellite Application Facility (OSISAF) used in SICCI Phase 2. For mean sea-surface (MSS) height product the previously used, provided by the Danish Technical University (DTU) in its 2015 version, has been updated to the 2018 version.

A summary of all used auxiliary data sets for the production of the sea-ice thickness climate data record is presented in Table 2-1.

3 OVERVIEW OF THE SIT PROCESSING CHAIN

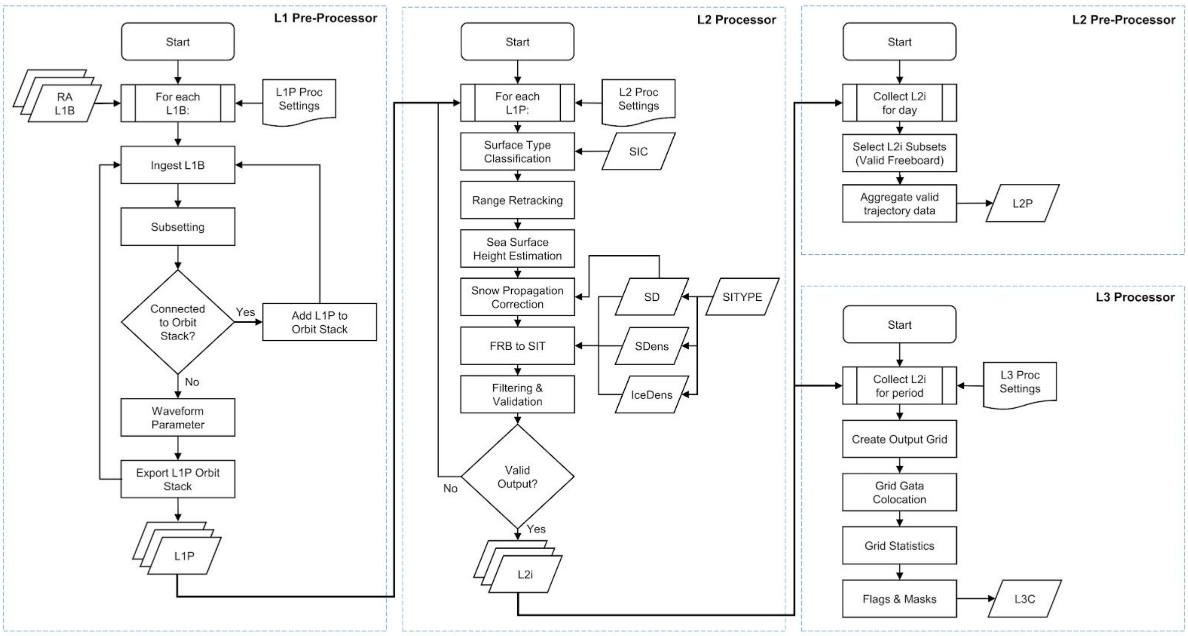

Figure 3-1: Flow chart for the Sea Ice Thickness Processor

Figure 3-1 presents an overview about the sea-ice thickness processing chain detailed into defined processors for the successive product data levels. The structure of the following sections is modeled after these processors that include details for each sensor. The geophysical retrieval starts with the surface-type classification, with the corresponding parametrization for Envisat RA-2, CryoSat-2 and ERS-1 and ERS-2. This continues with a thorough description of the range retracking procedure and a necessary Envisat RA-2 backscatter correction. Furthermore, the processing chain of radar freeboard and sea-surface height derivation, the estimation of sea-ice freeboard, and the estimation of sea-ice thickness are described. The subsections contain the computation of the geophysical parameters as well as the corresponding uncertainties.

While the geophysical retrieval is implemented at full sensor resolution, the aggregation of the parameter to space-time grids is described in the following sections of this document.

The processors are implemented in the python sea-ice radar altimetry toolbox (pysiral). This open source software project is hosted at Github (https://github.com/shendric/pysiral) and allows the inspection of the actual implementation of all algorithm components.

4 PRE-PROCESSING AND PRIMARY DATA (LEVEL-1 PRE-PROCESSING)

The main purpose of the pre-processing of the primary level-1 data is to provide a unified input format and data conventions for the following geophysical retrieval.

4.1 General Filtering

There is some sensor-specific general filtering applied, which follows UCL's implementation of the Envisat algorithm used during phase 1. This filtering is based on the available flags in the Envisat data indicating any significant problems with any record. In UCL's implementation of the filtering for Envisat, the Measurement Confidence Data Flags (MCD Flags) in the SGDR data are examined for problem records. We remove records where the following flags are raised: 0 (Packet Length Error), 1 (OBDH invalid), 4 (AGC Fault), 5 (Rx Delay Fault) and 6 (Waveform Fault).

For CryoSat-2 level-1b data, no general filtering mechanisms are necessary. For ERS-1 / 2 this is yet to be confirmed.

4.2 Region Filtering

The latitudinal boundaries within which Arctic and Antarctic sea ice is found are listed in the Table 4-1. The latitude values in the satellite data are examined and any data points outside these regions are rejected from the processing. The surface type flag in the data is also examined and any data not flagged as over ocean is also rejected.

Table 4-1: The table lists the latitudinal boundaries for the northern and southern hemisphere used for the region filtering

Area	Minimum Latitude	Maximum Latitude
Arctic	45.0	90.0
Antarctic	-90.0	-45.0

The data is cropped to the two latitude range and data over land masses are excluded, except if the orbit segment over land is shorter than 300 km. Else, the orbit is split into two segments.

4.3 CryoSat-2 Radar Modes

Only for CryoSat-2, the altimeter data is divided into orbit segments in three radar modes: LRM, SAR and SARIn. These come in separate product files, which are merged in the pre-processor. The merging process requires to reduce the SIN waveforms from 512 to 256 range bins of the SAR waveforms. This can be done without losing waveform information as the sea ice waveforms are narrow and defined. The step is unique to CryoSat-2, as other platforms (ERS-1/2, Envisat) provide data with a single radar mode.

4.4 Orbit Merging

Adjacent neighbouring orbit segments are merged into a single orbit segment over the polar regions whenever possible to enable consistent sea surface height estimation across the Arctic polar basin. Due to the geography in the Antarctic, the descending and ascending orbit segments over the ocean will always be separated by the Antarctic continent.

5 GEOPHYSICAL RETRIEVAL (LEVEL-2 PROCESSING)

The level-2 processing step includes the retrieval of the geophysical variables from the pre-processed radar measurements, with the use of auxiliary data listed in Table 2-1.

5.1 Surface-Type Classification

The surface-type classification is a crucial part in the processing chain of deriving sea-ice freeboard (and therefore sea-ice thickness), as the detection of leads is pivotal for determining the sea-surface height. The sea-surface height in turn is used as the reference from which the sea-ice freeboard is calculated. Additionally, a clear distinction between leads, sea ice and ambiguous mixed signals (which will be excluded from the actual freeboard retrieval) helps to improve the quality and accuracy of resulting sea-ice freeboard estimates. In other words, a surface-type selection bias is very likely to also have an impact on the resulting sea-ice freeboard and hence also the sea-ice thickness.

In general, with smaller instrument footprint sizes, less surface-type mixing occurs. However, leads often dominate acquired waveforms due to their specular reflection, and therefore act as sources of strong off-nadir backscatter signals. These off-nadir leads can substantially decrease the quality of the range retracking and increase the sensors' footprint. This is especially true for pulse-limited radar altimeters. In case of Envisat RA-2, the nominal circular footprint of 2 km in diameter (Connor et al., 2009) can increase to up to 10 km (Chelton et al., 2001) for strong off-nadir backscatter sources. Despite its much smaller footprint (1.65 km × 0.30 km), CryoSat-2 can also be affected by off-nadir leads, which will result in erroneous freeboard estimates (Armitage and Davidson, 2014).

5.1.1 Procedure Description

The surface classification algorithm is based on a multi-parameter classification based on a consistent set of parameters for ERS-1, ERS-2, Envisat RA-2 and CryoSat-2. The set of classifiers is defined by the sea-ice backscatter (SIG0), the leading-edge width (LEW) and the pulse peakiness (PP) as classifiers to positively identify between lead-type and sea-ice-type from otherwise ambiguous-type waveforms.

The pulse peakiness is subtly differently defined compared to the one used during phase 1 for Envisat RA-2 and follows the definition of Ricker et al. (2014):

$$PP = \sum_{i=1}^{N_{WF}} \frac{max(WF)}{WF_i} \cdot N_{WF}$$

The leading-edge width is defined as the width in range bins along the power rise to the first maximum between 5 % and 95 % of the first-maximum peak power while using a ten-times oversampled waveform.

The choice for using three classifiers also allows for less strict thresholds and was developed during CCI phase 2 and improved the previously used single threshold parameter classification for Envisat RA-2 during phase 1.

Over the course of a winter season, ice conditions can change substantially. Similar to leads, young and thin-ice areas feature rather specular reflections compared to other ice types. Furthermore, the amount of leads varies seasonally and regionally. Based on fixed thresholds for a whole winter season, these changes are difficult to capture and the rejection rate is increased unnecessarily. Hence, we decided on using monthly thresholds to improve the overall results and data quality.

There is a general lack of ground-truth data as collocated measurements of the same sea-ice situation are very difficult due to sea-ice drift and therefore rare. However, received waveforms feature very distinct characteristics and are well described in literature for sea ice and leads. These characteristics can also be deduced from the chosen set of classifiers. In order to bypass the lack of ground-truth, we decided to use a combination of unsupervised clustering and supervised classification.

Based on this combination, we are able to determine suitable thresholds for data acquired by Envisat RA-2 as well as CryoSat-2. The results seem to be promising for ERS-1 and ERS-2 as well, and are to improve more within the next iteration.The workflow of how we derived the surface-type thresholds is summarized in Figure 5-1.

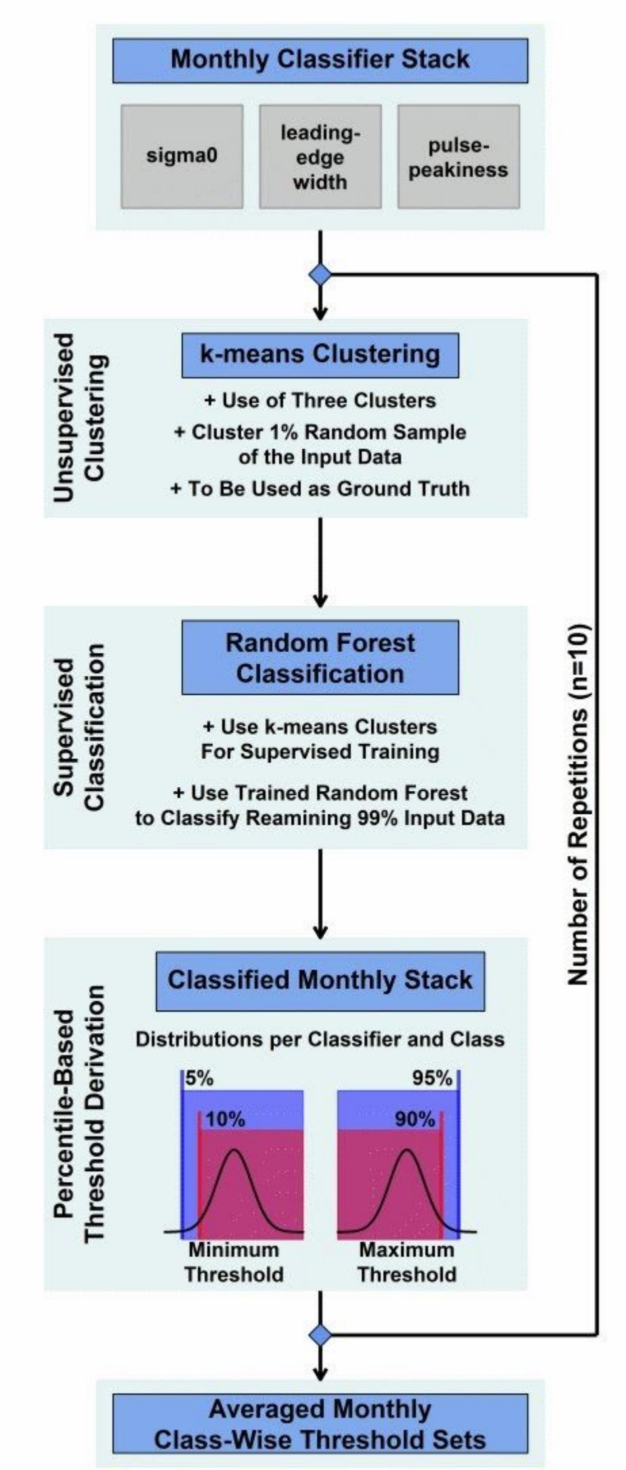

Figure 5‑1: Flowchart for the process of deriving thresholds for the new surface-type classification

In a first step, the three classifiers are computed for all available L1b data per sensor and month in the sensor overlap period from January 1995 to June 1996 for ERS-1 and ERS-2, from May 2002 to July 2003 for ERS-2 and Envisat and from November 2010 to March 2012 for Envisat and CryoSat-2. We only use waveforms that are located between 70°N and

81.5°N for the Arctic, are obtained over the ocean, and feature a minimum sea-ice concentration of 70%. The northern limit of 81.5°N was chosen to assure a maximum of consistency between Envisat RA-2 and CryoSat-2. In order to retrieve thresholds for the "Wingham Box" and other Arctic areas that are covered while CryoSat-2 operates in SIN mode, all waveforms above 70°N were used. For the Antarctic the same parameters apply, but waveforms are geographically limited to an area south of 65°S.

Next, 1 % of this monthly data are sampled randomly. This data sample is then separated into three clusters using k-means clustering (MacQueen et al., 1967; Hartigan et al., 1979). This methodology is widely used to separate input data of N observations into K clusters of equal variance, whereby the within-cluster sum-of-squares are minimized (MacQueen et al., 1967; Hartigan et al., 1979).

Generally, the preselection of the number of clusters can be a problem when utilizing k-means clustering. However, while we also tested a higher number of initial clusters with the perspective of later reunion of very similar clusters, a separation into just three classes turned out to be sufficient. Overall, lead waveforms account for a smaller fraction of the total measurements compared to sea-ice waveforms. Because of that and the fact that k-means clustering generally tends toward generating equal-size clusters (this is generally a presumption of k-mean algorithms), sole use of k-means clustering for the complete data set was not feasible.

This information in mind, the clustered 1 % data sample is therefore used as training data to train a random forest (Breiman, 2001). Random forests are an ensemble machine learning methods used for classification and are based on a large number of single decision trees that are fitted to randomized sub samples of the given training data set (Breiman, 2001). After initial training, the random forest can then be used for classification of the remaining data. Each tree in the trained forest then does a classification and casts a unique vote. In the end, the majority decides the resulting class. Each decision tree is thereby grown following certain rules: First, from the training data of size ***N***, ***N*** cases are sampled randomly with replacement as specific training data set for each single tree. Second, for ***M*** input parameters (in our case sea-ice backscatter, pulse peakiness, and leading-edge width), a fixed number ***m<<M*** of the given input parameters is specified and randomly selected out of ***M***. The best split on these selected parameters m is then used to split the node. Throughout the growing of the forest, the value of m is held constant. Third, each tree is grown out fully, i.e., to its largest possible extent. No pruning is applied. In contrast to single decision trees that tend to overfit, random forests do not overfit and are also capable of dealing with unbalanced data sets (Breiman, 2001).

For the here-used classification problem, we always grow a total number of 500 decision trees per training. Due to the small number of input parameters (**M**=3), we set **m** to one.

The trained random forest for each month is then used to classify the remaining 99 % of the corresponding monthly data. From this classified data set, distributions for each of the three classifiers for each month in the sensor overlap period are obtained. These distributions feature clear distinctions along each classifier's respective total range for each surface-type class (leads, sea ice, and ambiguous). Sea-ice backscatter is on average in the upper part of the range for the lead class and in the lower for the sea-ice class. Similar observations are apparent for pulse peakiness (upper part for leads, lower for sea ice) and leading-edge width (lower part for leads, upper part for sea ice). In other words, leads feature higher sea-ice backscatter and pulse peakiness as well as shorter leading-edge widths. The opposite is seen in the sea-ice class. The class of ambiguous signals is placed in between.

Thresholds are then obtained from the resulting classifier distributions by using either the 5 % or 10 % percentile for a minimum threshold, or the 90 % or 95 % percentile in case of a maximum threshold. The choice of using the more strict (10 %/90 %) or less strict (5 %/95 %) percentile thresholds depends on the sensor. Due to its larger footprint and therefore an expected higher degree of surface-type mixing, we chose the more strict thresholds for Envisat RA-2, and the less strict thresholds for CryoSat-2 due to its smaller footprint. For example, in order to derive thresholds for the detection of leads, the 5 %/10 % percentiles of the sea-ice backscatter and pulse-peakiness distributions would be used alongside the 90 %/95 % percentile of the leading-edge-width distribution. The final thresholds for ERS-1 and ERS-2 are yet to be determined, but initial versions are included in Tables 5-1 through Table 5-5.

The whole procedure, starting with randomly sampling 1 % from the initial monthly stack, is then repeated ten times. In a last step, the average minimum/maximum thresholds for each classifier, surface-type class, and month in the sensor overlap period are estimated. These thresholds are summarized in Table 5-1 through Table 5-5 and are used for all months in the complete climate data record.

Table 5-1: Metrics for ocean surface-type classification of waveform data for all sensors, hemispheres, and radar modes

Metric	Min	Max
Ocean waveforms are characterized by medium to low pulse peakiness (PP) values.		5
Only regions of very low ice concentration (SIC in %) values are suitable for the ocean surface type flag		5

Table 5-2: Metrics for lead surface-type classification of Envisat RA-2, CryoSat-2 SAR mode, and CryoSat-2 SIN mode waveform data for the Arctic

Metric	Month	ERS-1 RA		ERS-2 RA		Envisat RA-2		CryoSat-2 SAR		CryoSat-2 SIN	
		Min	Max	Min	Max	Min	Max	Min	Max	Min	Max
Lead waveforms are characterized by strong pulse peakiness (PP)	JAN FEB MAR APR OCT NOV DEC	16.36 16.72 17.02 17.17 16.68 18.22 16.97		20.96 20.51 20.55 20.73 23.25 22.32 21.45		46.90 46.40 46.20 48.40 52.90 51.00 47.70		67.30 66.30 66.60 69.90 76.00 73.80 68.60		264.30 257.90 253.60 264.60 291.80 288.80 272.60	
Lead waveforms are also characterized by high backscatter values due to specular reflection (SIG0)	JAN FEB MAR APR OCT NOV DEC	24.95 24.35 25.10 24.78 28.52 26.78 25.21		27.45 26.93 27.10 27.92 32.75 29.68 27.99		28.80 28.60 28.50 28.40 32.80 30.80 29.30		23.80 23.20 23.30 23.40 28.00 25.80 24.10		24.90 25.00 24.10 24.50 29.00 27.40 25.80	
Lead	JAN		1.18		0.97		0.82		0.77		1.10

waveforms feature a very steep increase in echo power and therefore short leading-edge widths (LEW)	FEB MAR APR OCT NOV DEC		1.17 1.16 1.18 1.22 1.15 1.17		0.98 0.98 0.99 0.94 0.95 0.96		0.82 0.82 0.82 0.82 0.82 0.82		0.78 0.78 0.76 0.72 0.73 0.76		1.11 1.13 1.09 1.02 1.03 1.07
Only lead classifications by waveform are expected that fall into regions of sufficient ice cover (checked with SIC in %)	JAN FEB MAR APR OCT NOV DEC	70 70 70 70 70 70 70		70 70 70 70 70 70 70		70 70 70 70 70 70 70		70 70 70 70 70 70 70		70 70 70 70 70 70 70	

Table 5-3: Metrics for sea-ice surface-type classification of Envisat RA-2, CryoSat-2 SAR mode, and CryoSat-2 SIN mode waveform data for the Arctic

Metric	Month	ERS-1 RA		ERS-2 RA		Envisat RA-2		CryoSat-2 SAR		CryoSat-2 SIN	
		Min	Max	Min	Max	Min	Max	Min	Max	Min	Max
Sea-ice waveforms shouldn't be peaky and therefore have a low pulse peakiness (PP)	JAN FEB MAR APR OCT NOV DEC		7.56 7.66 7.80 8.06 6.72 8.32 7.77		12.34 11.69 11.75 12.38 15.04 13.62 12.89		16.00 14.80 14.10 14.20 19.40 19.30 16.90		30.50 28.70 28.10 28.50 35.40 34.90 31.90		99.40 94.20 89.90 90.00 114.40 113.90 103.80
Sea-ice waveforms are also characterized by low backscatter values due to diffuse reflection (SIG0)	JAN FEB MAR APR OCT NOV DEC	9.69 9.70 9.43 9.03 10.02 10.23 9.90	17.75 17.76 17.20 16.75 18.85 18.90 17.99	14.68 13.98 14.19 14.09 17.94 15.82 15.22	22.87 22.23 22.13 22.52 27.09 24.65 23.57	2.5 2.5 2.5 2.5 2.5 2.5 2.5	22.50 21.80 21.30 20.40 25.90 24.60 22.80	2.5 2.5 2.5 2.5 2.5 2.5 2.5	20.80 19.90 19.60 19.00 25.70 23.20 21.10	2.5 2.5 2.5 2.5 2.5 2.5 2.5	21.40 20.90 20.10 19.10 24.30 23.70 22.00
Sea-ice waveforms feature a less steep increase in echo power and therefore longer leading-edge	JAN FEB MAR APR OCT NOV DEC	0.90 0.90 0.90 0.90 0.93 0.89 0.89		0.85 0.85 0.85 0.85 0.83 0.83 0.84		0.81 0.83 0.83 0.83 0.78 0.78 0.80		1.02 1.08 1.10 1.11 0.91 0.90 0.97			1.55 1.58 1.62 1.64 1.44 1.44 1.51

widths (LEW)											
Only sea-ice classifications by waveform are expected that fall into regions of sufficient ice cover (checked with SIC in %)	JAN FEB MAR APR OCT NOV DEC	70 70 70 70 70 70 70		70 70 70 70 70 70 70		70 70 70 70 70 70 70		70 70 70 70 70 70 70		70 70 70 70 70 70 70	

Table 5-4: Metrics for lead surface-type classification of Envisat RA-2, CryoSat-2 SAR mode, and CryoSat-2 SIN mode waveform data for the Antarctic

Metric	Month	ERS-1 RA		ERS-2 RA		Envisat RA-2		CryoSat-2 SAR		CryoSat-2 SIN	
		Min	Max	Min	Max	Min	Max	Min	Max	Min	Max
Lead waveforms are characterized by strong pulse peakiness (PP)	JAN FEB MAR APR MAY JUN JUL AUG SEP OCT NOV DEC	19.57 20.48 22.23 18.67 18.66 17.87 18.67 18.90 18.57 19.51 21.23 20.04		23.41 22.77 22.09 22.35 22.21 22.53 22.44 22.34 23.06 22.92 22.62 23.69		56.60 53.20 51.90 50.70 50.10 49.30 49.50 49.10 49.30 51.60 53.90 55.10		80.70 75.10 73.20 69.50 69.70 69.30 69.20 69.50 69.70 71.70 76.00 78.10		307.40 300.70 291.70 288.50 283.70 284.20 276.90 284.40 278.90 289.40 299.40 307.70	
Lead waveforms are also characterized by high backscatter values due to specular reflection (SIG0)	JAN FEB MAR APR MAY JUN JUL AUG SEP OCT NOV DEC	28.21 28.96 28.59 23.42 24.11 24.25 22.82 23.31 24.15 24.47 25.81 26.92		32.98 32.85 31.22 29.19 29.20 28.42 27.28 27.28 28.00 28.91 30.22 31.80		33.20 32.10 31.80 30.80 29.40 28.60 28.60 28.40 28.50 29.50 31.10 32.10		28.50 26.80 26.20 24.60 23.40 22.80 23.00 23.00 23.20 24.00 25.90 27.30		29.20 29.00 28.50 27.80 26.90 26.50 26.30 27.00 26.20 27.20 27.50 28.40	
Lead waveforms feature a very steep increase in echo power and therefore short leading-edge widths (LEW)	JAN FEB MAR APR MAY JUN JUL AUG SEP OCT NOV DEC		1.10 1.06 0.97 1.06 1.09 1.13 1.08		0.95 0.96 0.96 0.95 0.95 0.95 0.95 0.95 0.94 0.95 0.94 0.93		0.82 0.82 0.82 0.82 0.82 0.82 0.82 0.82 0.82 0.82 0.82 0.82		0.71 0.73 0.74 0.77 0.77 0.77 0.78 0.77 0.77 0.76 0.74 0.72		1.00 1.01 1.03 1.04 1.06 1.05 1.07 1.05 1.07 1.05 1.02 1.00

			1.08 1.12 1.08 1.03 1.07								
Only lead classifications by waveform are expected that fall into regions of sufficient ice cover (checked with SIC in %)	JAN FEB MAR APR MAY JUN JUL AUG SEP OCT NOV DEC	70 70 70 70 70 70 70 70 70 70 70 70		70 70 70 70 70 70 70 70 70 70 70 70		70 70 70 70 70 70 70 70 70 70 70 70		70 70 70 70 70 70 70 70 70 70 70 70		70 70 70 70 70 70 70 70 70 70 70 70	

Table 5-5: Metrics for sea-ice surface-type classification of Envisat RA-2, CryoSat-2 SAR mode, and CryoSat-2 SIN mode waveform data for the Antarctic

Metric	Month	ERS-1 RA		ERS-2 RA		Envisat RA-2		CryoSat-2 SAR		CryoSat-2 SIN	
		Min	Max	Min	Max	Min	Max	Min	Max	Min	Max
Sea-ice waveforms shouldn't be peaky and therefore have a low pulse peakiness (PP)	JAN FEB MAR APR MAY JUN JUL AUG SEP OCT NOV DEC		5.21 4.78 4.61 5.73 6.98 7.29 6.92 7.03 8.22 7.20 7.31 6.16		14.34 12.86 13.65 14.05 13.78 13.89 13.91 13.71 13.92 14.13 14.89 15.13		24.60 20.70 19.60 18.80 17.50 16.90 16.60 16.10 16.30 18.10 20.70 22.80		40.10 35.30 32.90 30.20 28.70 28.90 28.10 28.00 28.40 29.60 34.10 36.60		138.40 126.10 124.90 127.30 122.20 121.00 114.90 115.80 114.30 121.20 126.50 135.20
Sea-ice waveforms are also characterized by low backscatter values due to diffuse reflection (SIG0)	JAN FEB MAR APR MAY JUN JUL AUG SEP OCT NOV DEC	8.98 9.14 8.94 8.57 8.61 8.44 8.00 8.19 8.78 8.11 8.02 8.69	16.17 15.20 15.63 15.15 16.54 16.88 15.73 15.97 17.45 16.53 17.02 16.82	13.54 12.87 14.20 15.47 15.93 15.25 14.58 14.96 15.03 15.65 16.28 16.57	26.86 25.61 25.40 25.03 25.07 24.33 23.05 23.22 23.61 24.33 26.05 28.01	2.5 2.5 2.5 2.5 2.5 2.5 2.5 2.5 2.5 2.5 2.5 2.5	27.20 25.40 26.70 27.20 24.60 23.10 22.50 21.70 22.30 23.30 25.20 26.10	2.5 2.5 2.5 2.5 2.5 2.5 2.5 2.5 2.5 2.5 2.5 2.5	26.30 24.10 25.10 26.20 23.10 20.90 20.20 19.10 20.00 20.60 22.90 23.90	2.5 2.5 2.5 2.5 2.5 2.5 2.5 2.5 2.5 2.5 2.5 2.5	26.40 25.10 27.60 27.30 24.90 24.20 24.10 24.90 23.70 25.00 25.20 25.00
Sea-ice waveforms feature a less steep increase in echo power and therefore longer	JAN FEB MAR APR MAY JUN JUL AUG SEP	0.94 0.96 0.98 0.95 0.90 0.91 0.91 0.91		0.85 0.86 0.85 0.84 0.84 0.84 0.84 0.84 0.84		0.78 0.80 0.80 0.80 0.81 0.80 0.80 0.81 0.81		0.87 0.95 0.98 1.02 1.07 1.07 1.12 1.13 1.11		1.31 1.40 1.37 1.34 1.37 1.38 1.41 1.41 1.42	

leading-edge widths (LEW)	OCT NOV DEC	0.90 0.92 0.93 0.94		0.84 0.84 0.84		0.80 0.79 0.78		1.08 0.95 0.92		1.38 1.36 1.33	
Only sea-ice classifications by waveform are expected that fall into regions of sufficient ice cover (checked with SIC in %)	JAN FEB MAR APR MAY JUN JUL AUG SEP OCT NOV DEC	70 70 70 70 70 70 70 70 70 70 70 70		70 70 70 70 70 70 70 70 70 70 70 70		70 70 70 70 70 70 70 70 70 70 70 70		70 70 70 70 70 70 70 70 70 70 70 70		70 70 70 70 70 70 70 70 70 70 70 70	

5.1.2 Results

Utilizing this new and sensor-consistent surface-type classification scheme results in overall much better agreement between CryoSat-2 and Envisat RA-2 for typical benchmarks.

Compared to the surface-type classification used during Phase 1 for Envisat RA-2, our less strict approach allows for substantially more wave forms being classified as either lead or sea-ice type that were otherwise rejected before. Additionally, where there was a very high fraction of lead detections compared to only a very small fraction of classified sea-ice type waveforms during Phase 1, the spatial patterns and distributions of these occurrences are now better in line with what one would expect. Furthermore, the intermission consistency for the Arctic as well as the Antarctic has improved substantially (Figure 5-2 and Figure 5-3; Figure 5-4 and Figure 5-5)

The increased number of valid waveforms has an additional positive side effect on the overall data record: It allows for a much higher spatial resolution to be used in the final gridded Level 3 product without any compromises on overall coverage. Here, we are now able to provide a 25 km (50 km) resolution gridded data set for the Arctic (Antarctic) compared to a 100 km one during Phase 1.

Direct comparisons of surface-type class fractions (i.e., either ambiguous, lead, or sea ice) over the course of the sensor overlap period reveal an overall very good agreement between CryoSat-2 and Envisat RA-2 (Figure 5-2 and Figure 5-3). While the fraction of lead- and sea-ice waveforms is on average slightly smaller for Envisat RA-2 than for CryoSat-2 (about 8 % for the Arctic and 10 % for the Antarctic), both sensors show a similar seasonal development in both hemispheres.

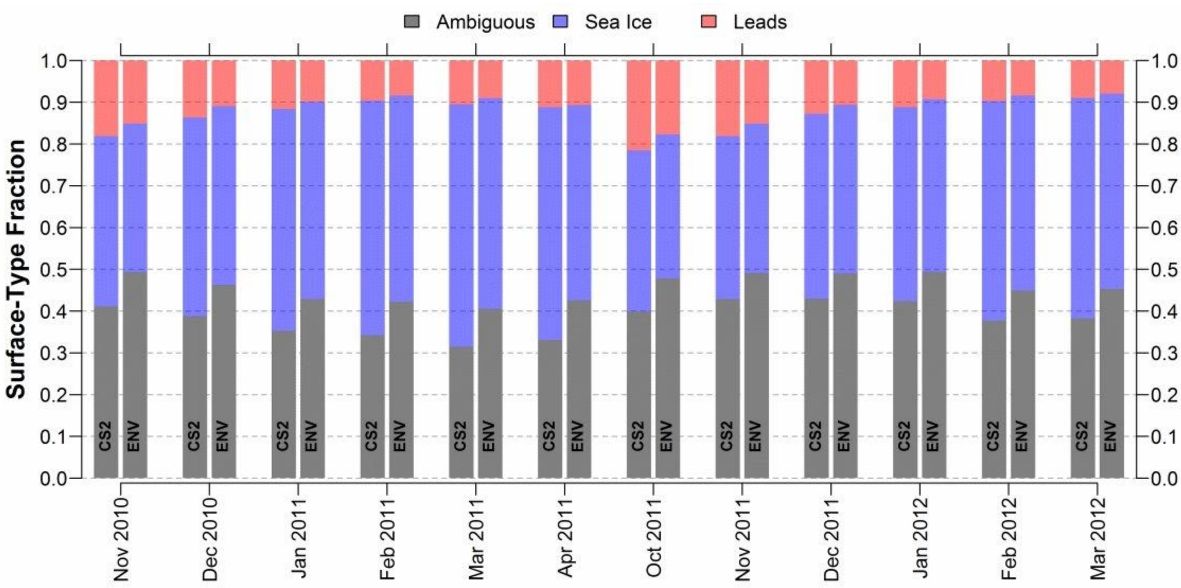

Figure 5‑2: Time-series of surface-type fractions for the sensor overlap period between CryoSat-2 (CS2) and Envisat RA-2 (ENV) for the Arctic

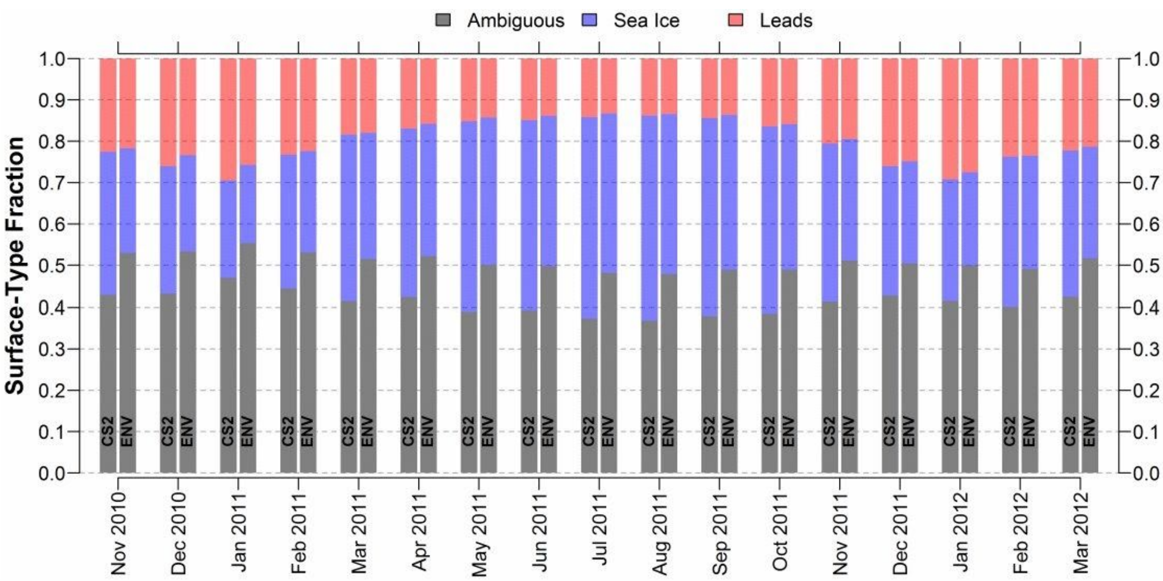

Figure 5‑3: Time-series of surface-type fractions for the sensor overlap period between CryoSat-2 (CS2) and Envisat RA-2 (ENV) for the Antarctic

This seasonal change in the present sea-ice cover is also apparent from the derived surface-type class thresholds (Table 5-1 - Table 5-5). During summer months (Antarctic) and the early winter (Arctic), the number of lead waveforms is higher and returns from new and young ice tend to be more specular, which results in higher maximum thresholds in sea-ice backscatter und pulse peakiness. This observed seasonal shift in the distributions of the classifiers will also play an important role in the description of the new retracker scheme.

An exemplary visualization of monthly map-wise inter-comparisons between Envisat RA-2 and CryoSat-2 based on the benchmarks of valid-, lead-, and sea-ice fraction is shown in Figure 5-4 and Figure 5-5. In these gridded data sets, the overall good agreement is confirmed. However, there are small differences, and as mentioned earlier, slightly smaller valid fractions for Envisat RA-2. This behavior is expected and results most likely from the much larger footprint of Envisat RA-2, especially in regions with high rates of sea-ice dynamics such as the Beaufort Sea, but also in the Laptev Sea. Here, the increased surface-type mixing likely prevents a clearer separation between waveform types.

Nevertheless, both comparisons highlight the overall good agreement that could be achieved between both sensors with this new surface-type classification scheme and the chosen settings during the sensor overlap period. These results therefore lay the foundation for a proper inter-mission sea-ice freeboard and sea-ice thickness data record.

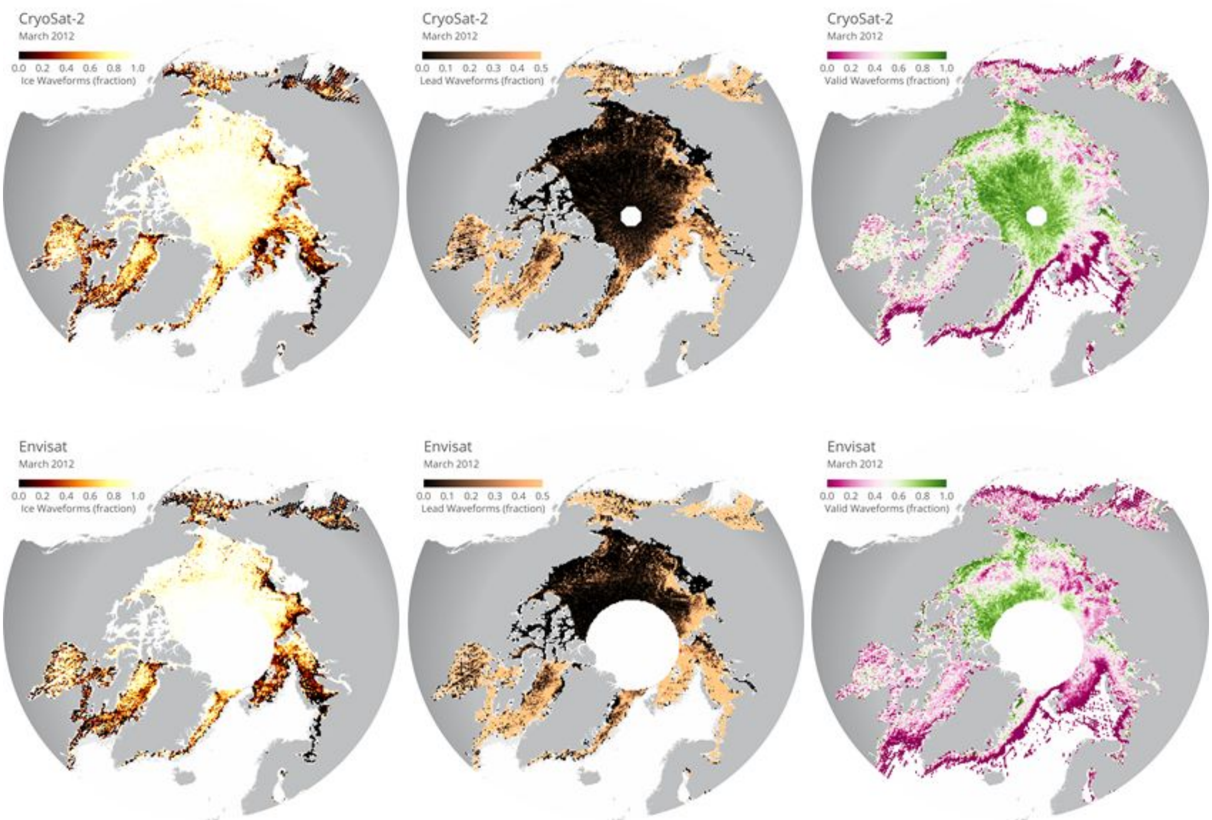

Figure 5-4: Visualizations of monthly sea-ice fraction, lead fraction, and valid fraction benchmarks for the Arctic (March 2012)

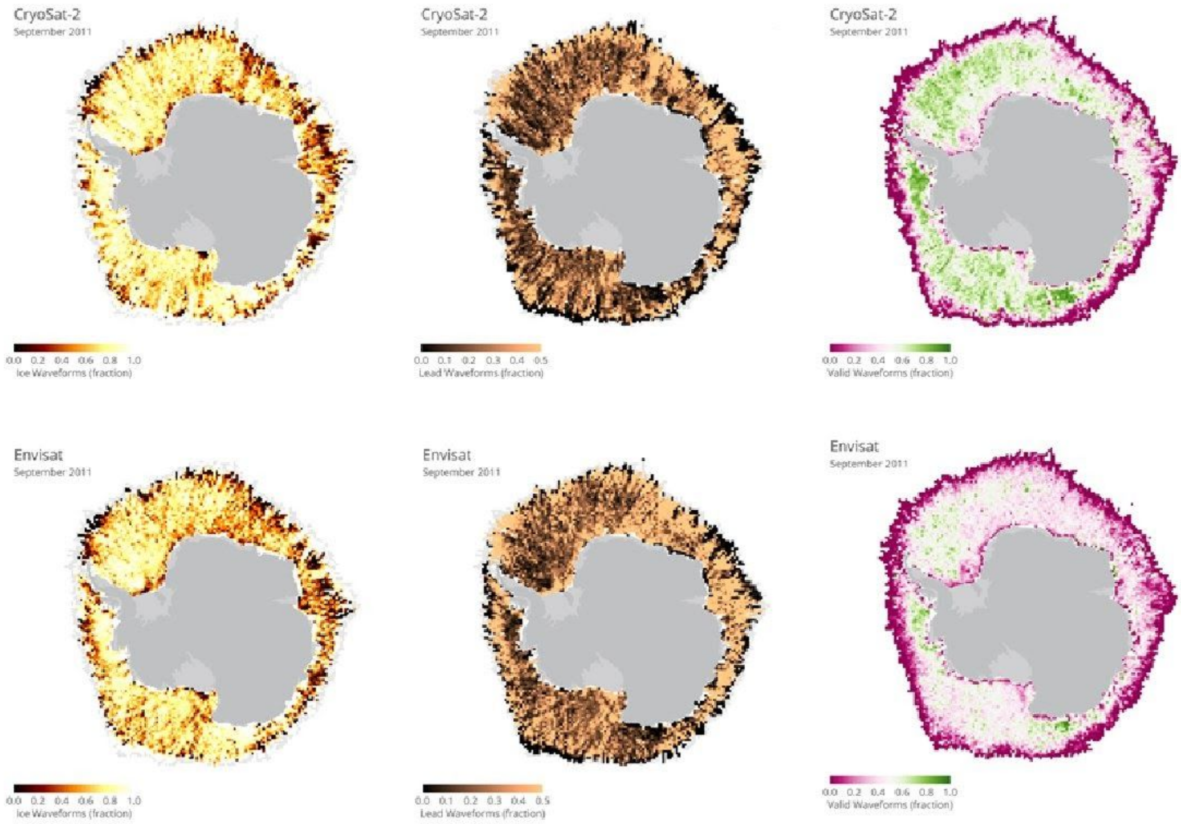

Figure 5‑5: Visualizations of monthly sea-ice fraction, lead fraction, and valid fraction benchmarks for the Antarctic (September 2011)

For ERS-1 and ERS-2, a similar procedure to analyze the surface type metrics shall be carried out in the same scale as for CryoSat-2 and Envisat. For this revision, we have included similar figures only for Arctic for ERS-2, where our main focus has been during the first year. Keep in mind that these are the results from the first attempt. Due to differences in instrument parameters (bin width, noise level etc.) we can notice differences in the metrics of ERS-2 when compared to those of Envisat, as in Figure 5-6. In ERS-2 there seems to be slightly more leads and only third of the ice that the Envisat processing catches. As can be seen in Figure 5-7, the fraction of ice waveforms appears to be smaller and the fraction of lead waveforms greater than one could expect. Fraction of valid waveforms is very low, and surprisingly lowest around the central Arctic. Differences between the metrics between

ERS-1 and ERS-2 are also to be expected, as well as between Arctic and Antarctic.

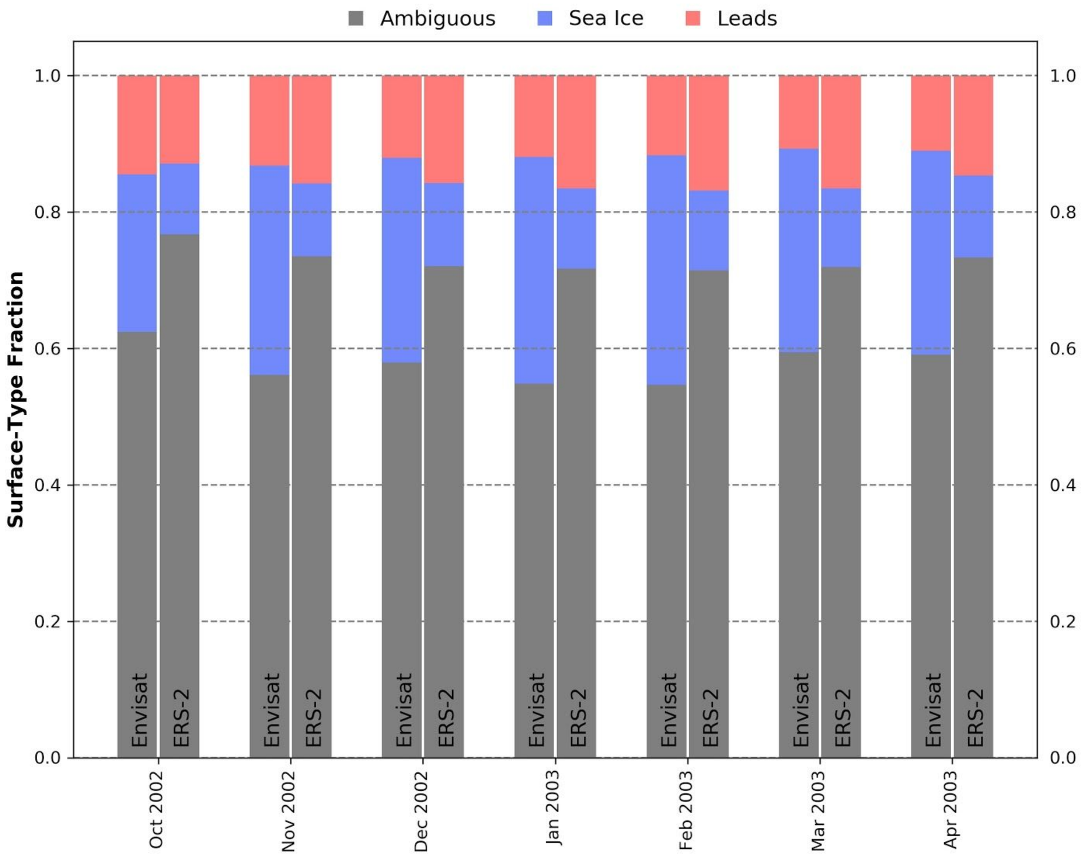

Figure 5‑6: Time-series of surface-type fractions for the sensor overlap period between Envisat RA-2 (Envisat) and ERS-2 RA (ERS-2) for the Arctic

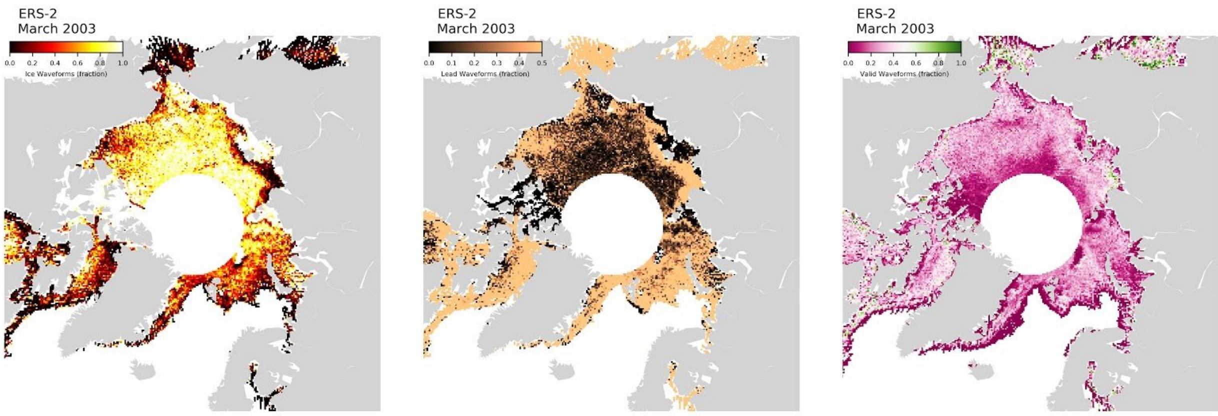

Figure 5‑7: Visualizations of monthly ERS-2 sea-ice fraction, lead fraction, and valid fraction benchmarks for the Arctic (March 2003)

5.2 Retracking

5.2.1 Procedure Description

The range retrieval algorithm for Envisat RA-2 and CryoSat-2 waveforms is identical for sea-ice and lead waveforms. Ocean waveforms are currently discarded. The used Threshold First Maximum Retracker Algorithm (TFMRA, Helm et al., 2014; Ricker et al, 2014) is based on the following steps:

a) Estimate the noise level as the average of the first 5 bins of the waveform. However, in case of Envisat RA-2 we are following UCL's implementation and discard the counts in the first 5 bins of the echo as these just contain artefacts of the FFT.

b) Oversampling of the echo waveforms by a factor of 10 using linear interpolation

c) Smoothing of the oversampled waveform with a window filter size of 11 range bins

d) Locating the first local maximum of the waveform: Must be higher than noise level + 15% of absolute peak power.

e) Obtain the range value at a specified threshold of the power of the detected first maximum, by linear interpolation of the smoothed and oversampled waveform.

Continuing on the last point, the choice of retracker threshold is pivotal for the range estimation. Following AWI's implementation for CryoSat-2 (Ricker et al., 2014), we keep a consistent threshold of 50% from the first maximum peak power both for leads and sea-ice waveforms. For pulse-limited altimetry such as for Envisat RA-2, retracking near the maximum power for leads proved to be essential to retrieve reasonable freeboard estimates later on. Therefore, a threshold of 95% was chosen for leads from Envisat RA-2 waveforms. However, using a single fixed threshold of, e.g., 50% similar to CryoSat-2, results later on in sea-ice freeboard estimates that feature an overall smaller variation than CryoSat-2 estimates. Furthermore, expected thin-ice regions feature ice that is too thick and vice versa. We relate this behavior to the much larger footprint and therefore increased mixing of surface types of different surface-roughness scales in every Envisat RA-2 waveform.

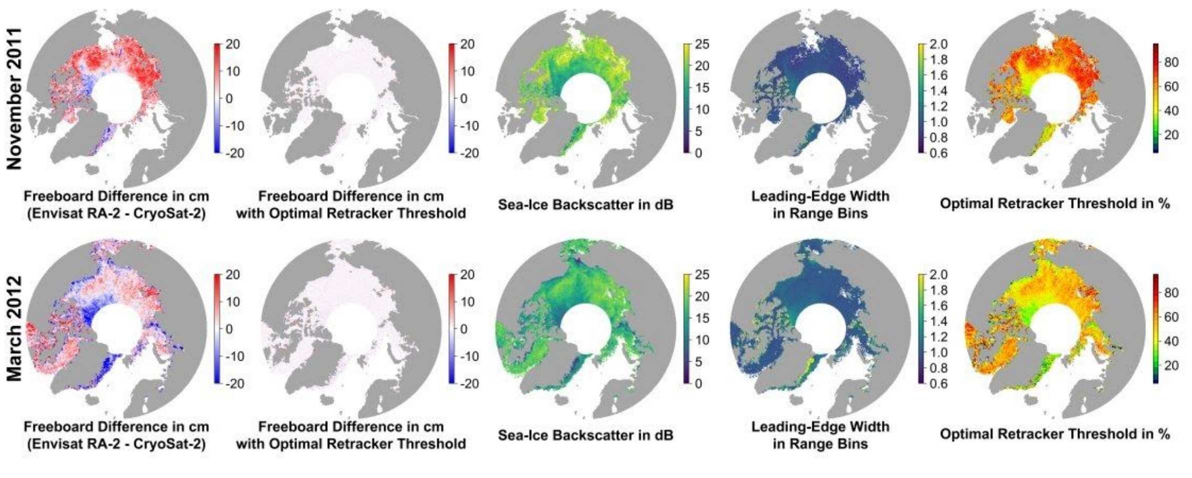

Figure 5-8: Visualizations of two monthly sets of figures (from left to right): Freeboard difference between Envisat RA-2 and CryoSat-2, the best achievable freeboard difference using an optimal retracker threshold, the sea-ice backscatter, the leading-edge width, and the iteratively estimated optimal threshold for November 2011 (top row) and March 2012 (bottom row)

From Figure 5-6 it appears that differences in sea-ice freeboard are related to differences in the waveform parameters of sea-ice backscatter and leading-edge width (as well as pulse peakiness, which is strongly correlated with sea-ice backscatter, but is not shown here). Areas of potential multi-year ice near the Canadian Archipelago and areas influenced by multi-year ice export are in general substantially too thin (e.g., about 20 cm and more in March), whereas areas of predominantly first-year sea ice are in general too thick in the Envisat RA-2 data. However, the level of freeboard difference appears to be seasonal, where Envisat RA-2 appears to be unable to keep track of these seasonal changes.

As these differences in sea-ice freeboard between CryoSat-2 and Envisat RA-2 appear to be indeed strongly correlated to patterns in the sea-ice backscatter and the leading-edge width of Envisat RA-2 waveforms, we decided to apply a tuning scheme by computing an adaptive range retracker threshold as a function of sea-ice backscatter and the leading-edge width to mitigate the differences. Due to the already mentioned larger footprint of Envisat RA-2 and hence increased mixing of different surface types, it appears to be necessary to treat waveforms differently according to the waveform shape (and hence surface properties) by means of retracking the main scattering horizon.

In order to derive the functional relationship between threshold and sea-ice backscatter/leading-edge width, we first processed all Envisat RA-2 for the complete sensor overlap period. This processing was done using the TFMRA with a fixed threshold for leads of 95 % and a threshold for sea-ice waveforms that was changed in each run. This sea-ice threshold ranged between 5 % and 95 % in steps of 5 %. For example, in the first run the complete data set was processed using a retracker threshold of 5 % for sea-ice waveforms and the resulting sea-ice freeboard was calculated. In the next run, a fixed threshold of 10 % was used for all sea-ice waveforms and so on, until the last run with a sea-ice threshold of 95 % was computed and the resulting sea-ice freeboard was calculated.

From this data set, the optimal threshold, i.e., the threshold that yields the smallest difference in freeboard between Envisat RA-2 and CryoSat-2, was iteratively derived. An exemplary result is also shown in Figure 5-6. Again, also the optimal thresholds reflect the seasonal change in waveform parameters with a varying range of optimal threshold values that are in general higher for the early winter than the values in late winter.

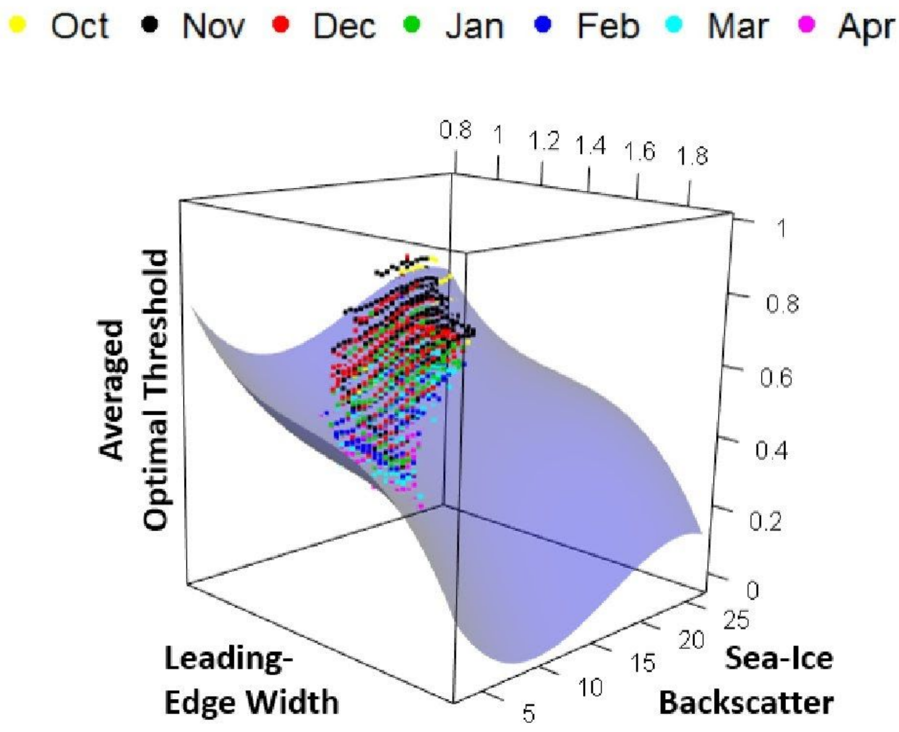

Figure 5-9: Visualizations of averaged binned optimal threshold values on an x-y plane of leading-edge width and sea-ice backscatter for the Arctic. The blue plane is the 3rd order polynomial fit through all data points

Next, average optimal threshold values were calculated for each 0.25 dB sea-ice backscatter and 0.025 leading-edge width bin on an x-y plane. A 3D visualization of this is shown in Figure 5-7. For months November through March both occurrences in the sensor overlap period were used. October and April, which were only covered once during the sensor overlap period were each added twice to circumvent issues of underrepresentation in their number of data values added to the total.

Through this compilation of monthly data points, three 3rd order polynomial planes were fitted based on different weighting schemes in order to maximize the adjusted R^2. As weights we used either the number of optimal threshold values per bin in the x-y plane, the inverse standard deviation of all optimal threshold values per bin ($1/\sigma$), or no weights at all.

For the Arctic, the result shown in Figure 5-7 is based on the inverse standard deviation as weights and achieved an adjusted R^2 of 0.94. All shown data points have a minimum of 50 occurrences and were obtained in the central Arctic only.

In Figure 5-7, the seasonal shift is also present: Early winter months tend towards shorter leading-edge widths and higher sea-ice backscatter values (October in yellow and November in Black), whereas late-winter months feature longer leading-edge widths and lower backscatter values.

The optimal threshold (th_{opt}; in decimal values) to be used in the adaptive range retracking as a function of sea-ice backscatter (σ^0) and leading-edge width (lew) is given by the following equation:

$$th_{opt} = k_1 - k_2 \times lew + k_3 \times lew^2 - k_4 \times lew^3 - k_5 \times \sigma^0 + k_6 \times \sigma^2 - k_7 \times \sigma^3$$

Where k_1 = 3.4775697362, k_2 = 5.9296875486, k_3 = 4.3516498381, k_4 = 1.0933131955, k_5 = 0.0914747272, k_6 = 0.0063983796, k_7 = 0.0001237455.

In a first attempt, we applied the same equation that was derived from the northern hemisphere data also to the southern hemisphere. However, this did not improve the results. The reason for that can partly be seen in Figure 5-8. In contrast to the Arctic, the differences between early and late winter is less prominent in the sea-ice freeboard differences as well as the optimal-threshold values. Additionally, patterns in sea-ice backscatter and leading-edge width are less correlated in some areas. This is potentially related to surface flooding and/or large fast-ice areas with a different snow stratigraphy.

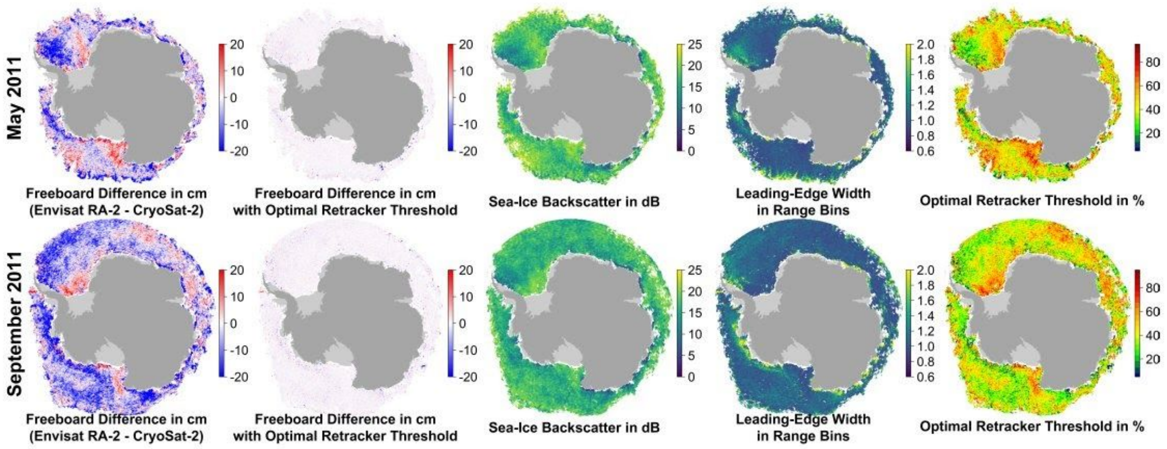

Figure 5-10: As Figure 2-12 but for the Antarctic showing May 2011 (top row) and September 2011 (bottom row)

For the Antarctic, a 2nd order polynomial fit resulted in the best statistical result (adjusted R^2 of 0.77) to describe the optimal threshold as a function of leading-edge width and sea-ice backscatter (Figure 5-8).

For the Antarctic, the result shown in Figure 5-9 is based on the number of optimal threshold values per bin as weights. All shown data points also have a minimum of 50 occurrences and were obtained by excluding the marginal ice zones of the Antarctic as well as the austral summer months. However, compared to the Arctic, there is a much larger spread between months.

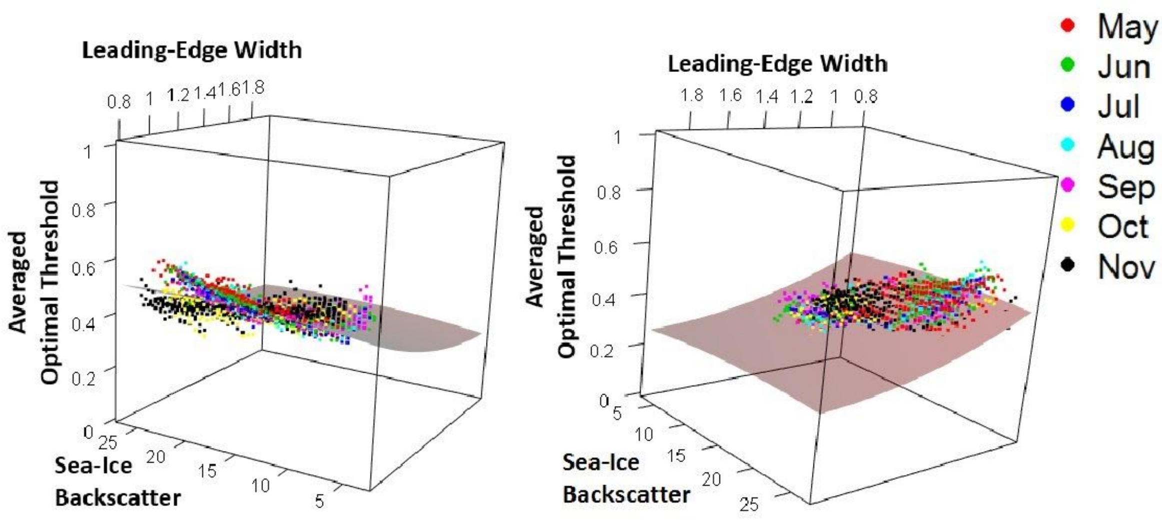

Figure 5-11: As Figure 2-13 but for the Antarctic and captured from two different viewpoints.

The equation to be used for deriving the optimal threshold (in decimal values) in the Antarctic adaptive range retracking as a function of sea-ice backscatter (σ^0) and leading-edge width (*lew*) is stated below:

$$th_{opt} = k_1 - k_2 \times lew + k_3 \times lew^2 + k_4 \times \sigma^0 - k_5 \times \sigma^{0^2}$$

Where k_1 = 0.8147895184, k_2 = 0.5555823623, k_3 = 0.1347526920, k_4 = 0.0055934198, k_5 = 0.0001431595

Utilizing both equations, for each retracking of each sea-ice waveform, the to-be-used threshold is calculated from the waveform-associated sea-ice backscatter and leading-edge width value. This threshold is then believed to yield the mean-scattering surface in accordance to CryoSat-2 measurements.

5.2.2 Results

Here, we want to show and discuss some of the results using the adaptive threshold retracker for Envisat RA-2 in the sensor overlap period. For the Arctic, Figure 5-10 shows the average freeboard in centimeters per month, the average freeboard difference in centimeters as well as percent during the sensor overlap period for Envisat RA-2 and CryoSat-2. While in the first winter season, the match is nearly perfect with absolute average freeboard differences below one centimeter, the second winter season shows larger differences.

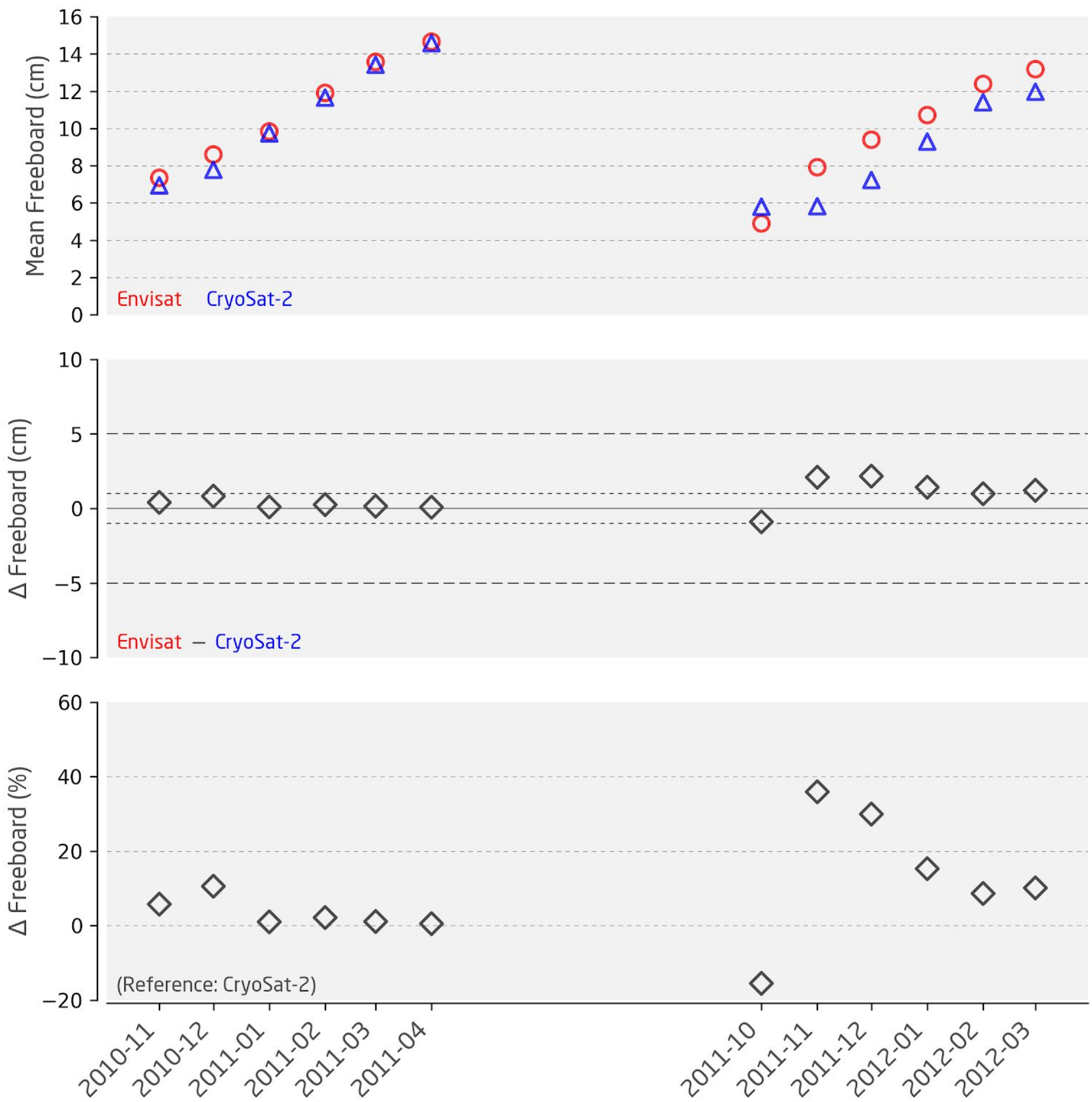

Figure 5-12: Mean freeboard for each month of the sensor overlap period (top) for Envisat RA-2 (red) and CryoSat-2 (blue) and the corresponding mean freeboard difference between both sensors in centimetres (middle) and percent with reference to CryoSat-2 (bottom) for the Arctic

However, these differences are still below three centimeters, which is a significant improvement over phase 1. Especially for the Arctic spring period (March & April), differences in average freeboard are 1.2 cm or better. The stability, i.e., the range of monthly differences, is 3.1 cm.

For the Antarctic, results are not as good as for the Arctic (Figure 5-11). Overall the algorithm has less skill to match Envisat RA-2 freeboards to the ones of CryoSat-2. This is very likely related to other physical processes such as more prominent snow stratigraphy and surface flooding. However, issues causing these differences are subject to further investigation. Overall, there is a stronger seasonality in the differences between summer and winter, which also leads toward a higher range of monthly differences of 4.6 cm.

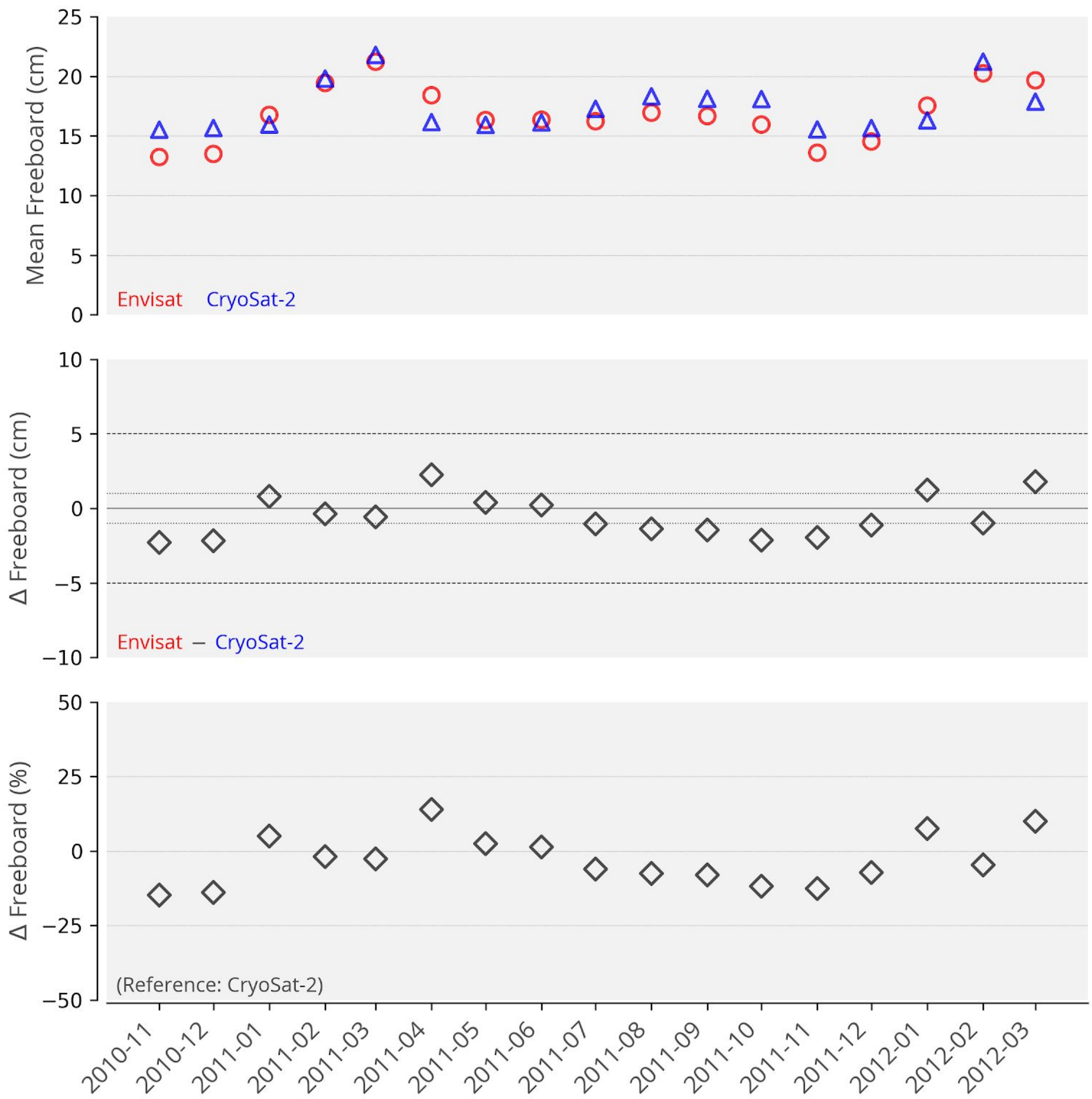

Figure 5-13: Setup as in Figure 5-10 but for the Antarctic

Putting all gridded freeboard values of Envisat RA-2 and CryoSat-2 against each other underlines these observations (Figure 5-12). While the algorithm is able to achieve very good agreement for the Arctic (Figure 5-12, left), the results are slightly more diffuse for the Antarctic (Figure 5-12, right).

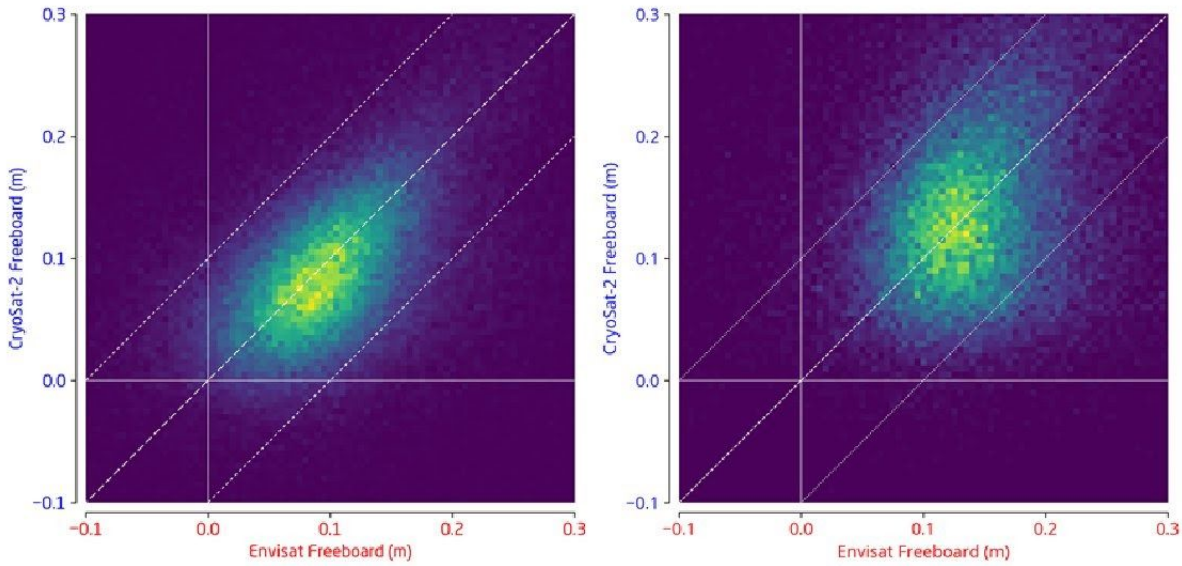

Figure 5-14: Scatterplot of all gridded freeboard estimates of CryoSat-2 (y-axis) vs. Envisat RA-2 (x-axis) for the Arctic (left) and the Antarctic (right).

5.2.3 Envisat Backscatter Drift Correction

Over the course of Envisat's life span, it appears that the RA-2 instrument has been degraded (Helm, 2017, pers. comm.). This results in a slight linear reduction in received backscatter over the years (Figure 5-13). As this can affect both the surface-type classification as well as the range retracking (as both are dependent on the received sea-ice backscatter), a correction had to be applied.

The monthly degradation factor of -0.003269253 was derived from the monthly averages of ocean-type waveforms in the Barents Sea (70°N-75°N and 40°E-50°E). Ocean-type waveforms are derived independent from the sea-ice backscatter classifier and we assume the surface roughness sufficiently random compared to ice-type waveforms for our analysis.

As the surface-type classification as well as the range retracking was derived from data in the sensor overlap period (November 2010 to March 2012), all backscatter values had to be corrected towards this base period. In order to accomplish that we picked June 2011 as a reference point.

Using the below given formula, we calculated the necessary backscatter drift correction:

$$t_{sift} = 12 \times (\alpha_{ref} - \alpha) + (m_{ref} - m)$$

$$\sigma^0_{drift} =- 0.003269253 \times t_{sift}$$

Here, t_{sift} is the time shift factor in months between the reference year (a_{ref}) and month (m_{ref}) and the currently processed year (a) and month (m). The resulting backscatter drift correction σ^0_{drift} is then added to the sea-ice backscatter before the surface-type classification and the range retracking. By doing so, the in general slightly higher backscatter values during earlier years of Envisat's lifespan are reduced to the level during the sensor overlap period.

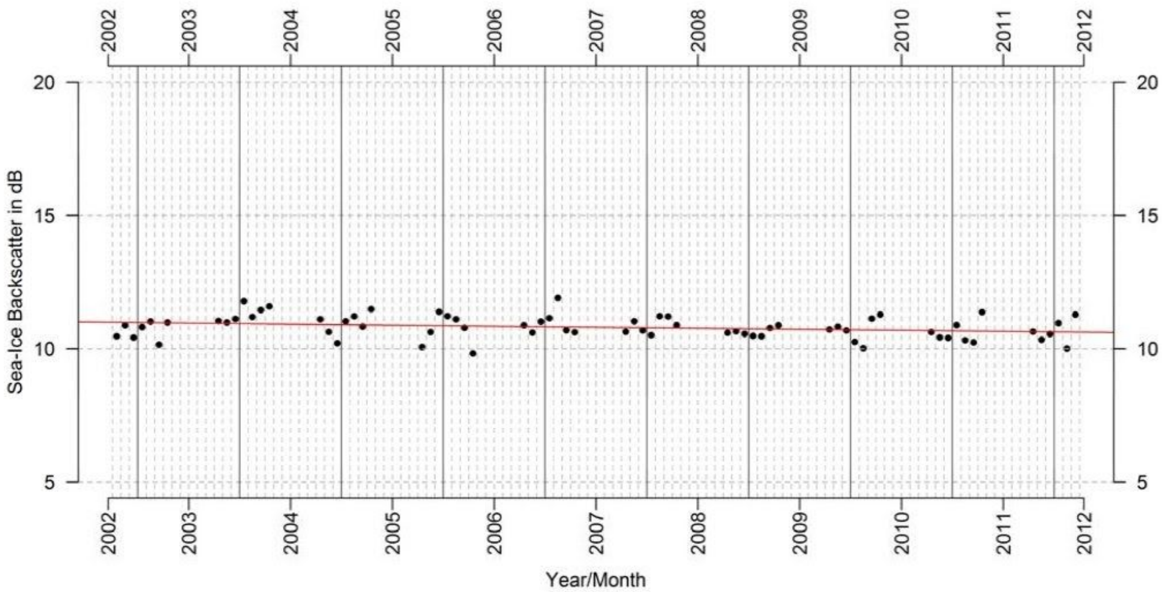

Figure 5-15: Visualizations of the monthly averaged sea-ice backscatter reduction between 2002 and 2012 over ocean-type waveforms obtained between 70°N-75°N and 40°E-50°E

5.2.4 ERS-1 and ERS-2 Retracking

For ERS-1 and ERS-2, adaptive retracker shall be used as well. Values for k_0 - k_6 (for the calculation of optimal threshold) shall be derived minimising the difference between ERS-2 and Envisat freeboards during the overlap period. Similarly, the ones for ERS-1 shall be derived from the ERS-1 and ERS-2 overlap period.

5.2.4.1 Pulse Deblurring

A significant challenge in ERS retracking is the pulse blurring which results from the range window moving during waveform averaging sequence. For detailed description of pulse blurring, see Peacock and Laxon (2004). A linear correction to the retracked range is applied if the height error signal $\varepsilon < 0$. Unfortunately, the ε is not present in the REAPER SGDR files used as input for the CCI+ processor. In consequence, the pulse deblurring correction must be derived elsewhere.

As a surrogate for the height error signal ε, first version of the pulse deblurring algorithm uses the delta_range which is the change in range from the nominal tracking point to the satellite between the waveform and previous one. For the N:th waveform, this can be written as:

delta_range(N) = range(N) - range(N-1)

When looking at the relationship of delta_range and the ERS-2 retrieved SLA (elevation - MSSH) there is a clear linear dependency for measurements with delta_range < 0. An example of SLA and delta_range from ERS-2 in January 2003 is shown in Figure 5-14 below:

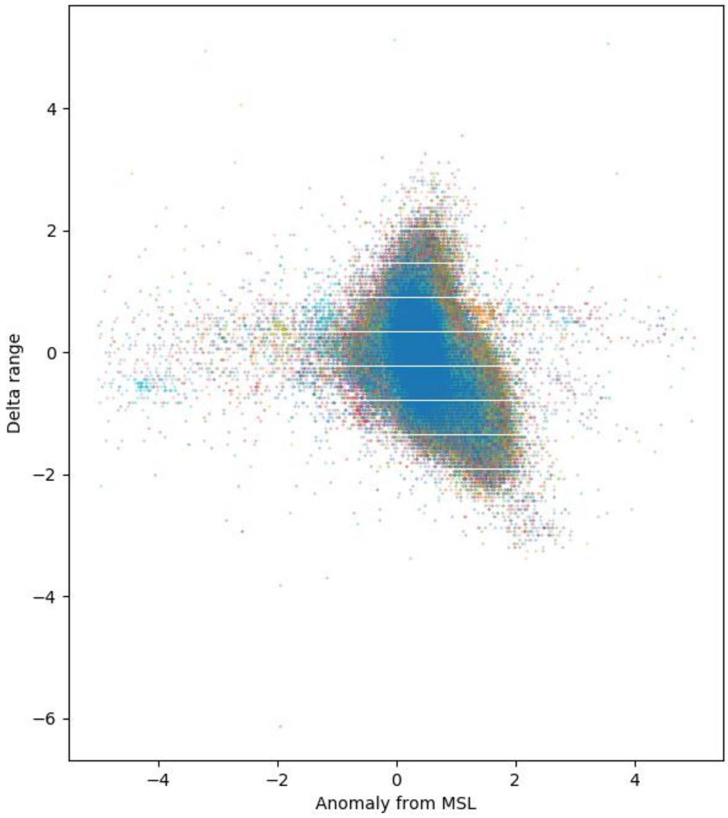

Figure 5-16: An example of SLA and delta_range from ERS-2.

As the two variables should not be correlated, we introduce a pulse deblurring correction delta_H to the retracted elevations of:

delta_H	= 0	if delta_range >= 0
	= m*delta_range	if delta_range < 0

Do derive *m*, we fitted a first degree polygon to the SLA / delta_range -data shown in Figure 5-14 above and arrived at m=0.344. However, as the correction will be sensitive to the retracker used, and possibly is not constant over the whole ERS2 period, more effort shall be put into refining the correction in the future.

The empirical deblurring above is just the first try, and the pulse deblurring may have to be defined in a similar manner to the adaptive retracker threshold - that is, finding an empirical correction that minimises the difference between ERS-2 and Envisat (and later ERS-1 and ERS-2) during the overlap period.

5.3 Geophysical Range Correction

The range is corrected for the changes in sea level due to tides and atmospheric pressure. The specific geophysical range corrections are:

- Elastic ocean tide
- Geocentric polar tide
- Long-period ocean tide
- Solid earth tide
- Inverse barometric correction

5.4 Radar Freeboard and Sea-Surface Height

The vast majority of the signal seen in the floe and lead elevations retracked in the last section is caused by unevenness in the Earth's gravity field and mean circulation of the ocean currents. This fixed signal known as the mean sea surface must be removed before any interpolation of the sea surface heights is attempted. Many models of the mean sea surface are available and there will almost certainly be one present in the satellite data product. It is however advisable to use a consistent mean sea surface height product based on altimeter data from the target period (1993-2020).

An example for such a global mean sea surface height product is DTU18 (Table 2-1), which is based on radar altimeter data from ERS-1 to CryoSat-2 and thus spans the target SIT ECV period and region. DTU18 is the improved version from the formerly used DTU15 mean sea surface height, which is visualized in Figure 5-15.

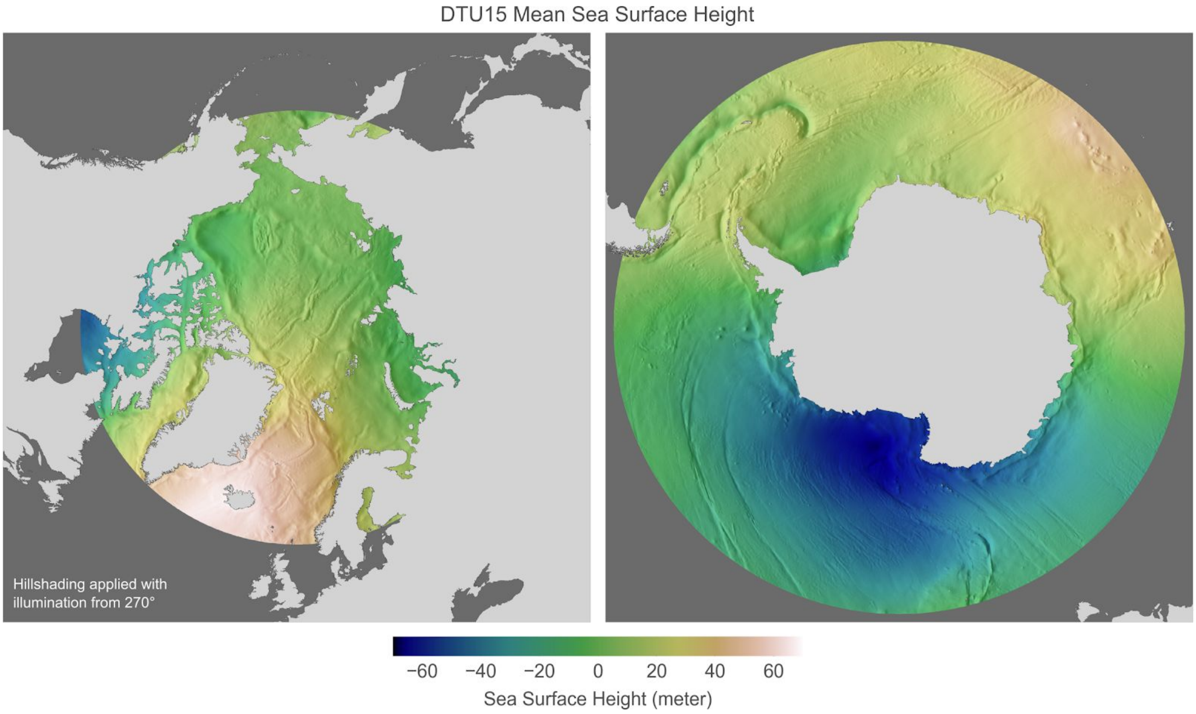

Figure 5-17: Hillshaded sea surface height of the DTU15 global mean sea surface height product for the SIT ECV target region in the northern and southern hemisphere

With the mean sea surface height removed from the sea surface heights in the leads, the remaining signal will be due to time variant changes in sea surface height caused by variability in the magnitude and direction of ocean currents; the dynamic topography and long wavelength errors in tides and atmospheric corrections. This signal varies on a scale of a few hundred kilometres. The ice freeboard, or the height the ice floe protrudes above the sea surface, is determined by interpolating the sea surface height beneath the floe location and subtracting it from the height of the floe. Figure 5-16 and Figure 5-17 illustrate this calculation. Practically, the residual of the lead elevations with respect to the mean sea surface height (MSSH) yield the sea surface height anomaly (SSHA). The instantaneous sea surface height (SSH) is then defined by

SSH = MSSH + SSHA

The sea surface height measurements are then linearly interpolated and smoothed by a box filter using a window size of 25 km. A minimum of one lead must exist for each orbit to allow a proper estimation of the instantaneous sea surface height. The result from subtracting the interpolated and smoothed sea-surface height from all retracked sea-ice elevations yields the radar freeboard (RFRB). Radar freeboard in contrast to the sea-ice freeboard is not corrected for the slower wave propagation speed in the snow layer and therefore biased low.

RFRB = ELEV_ice - SSH

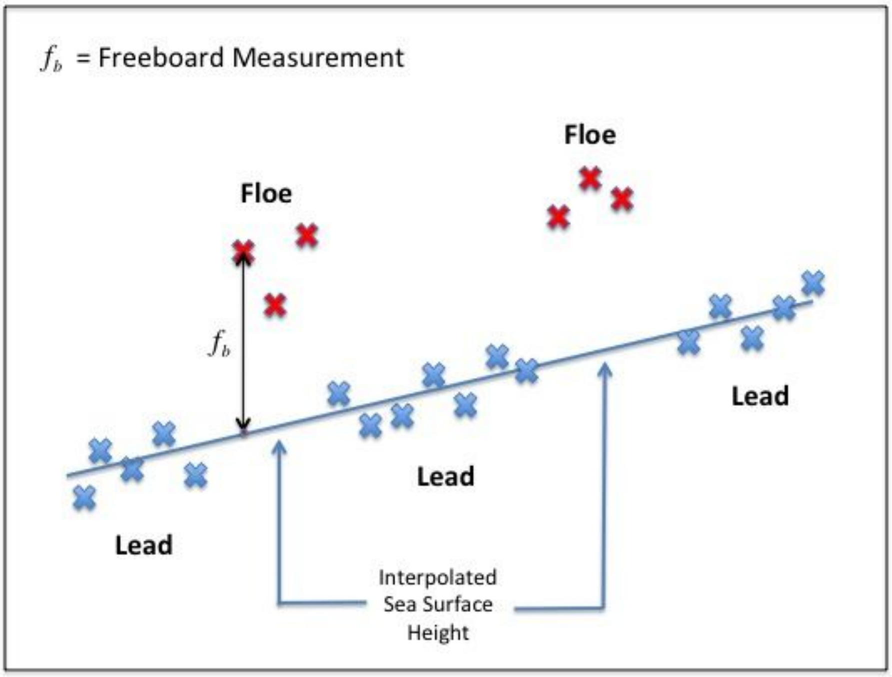

Figure 5-18: Computation of radar freeboard

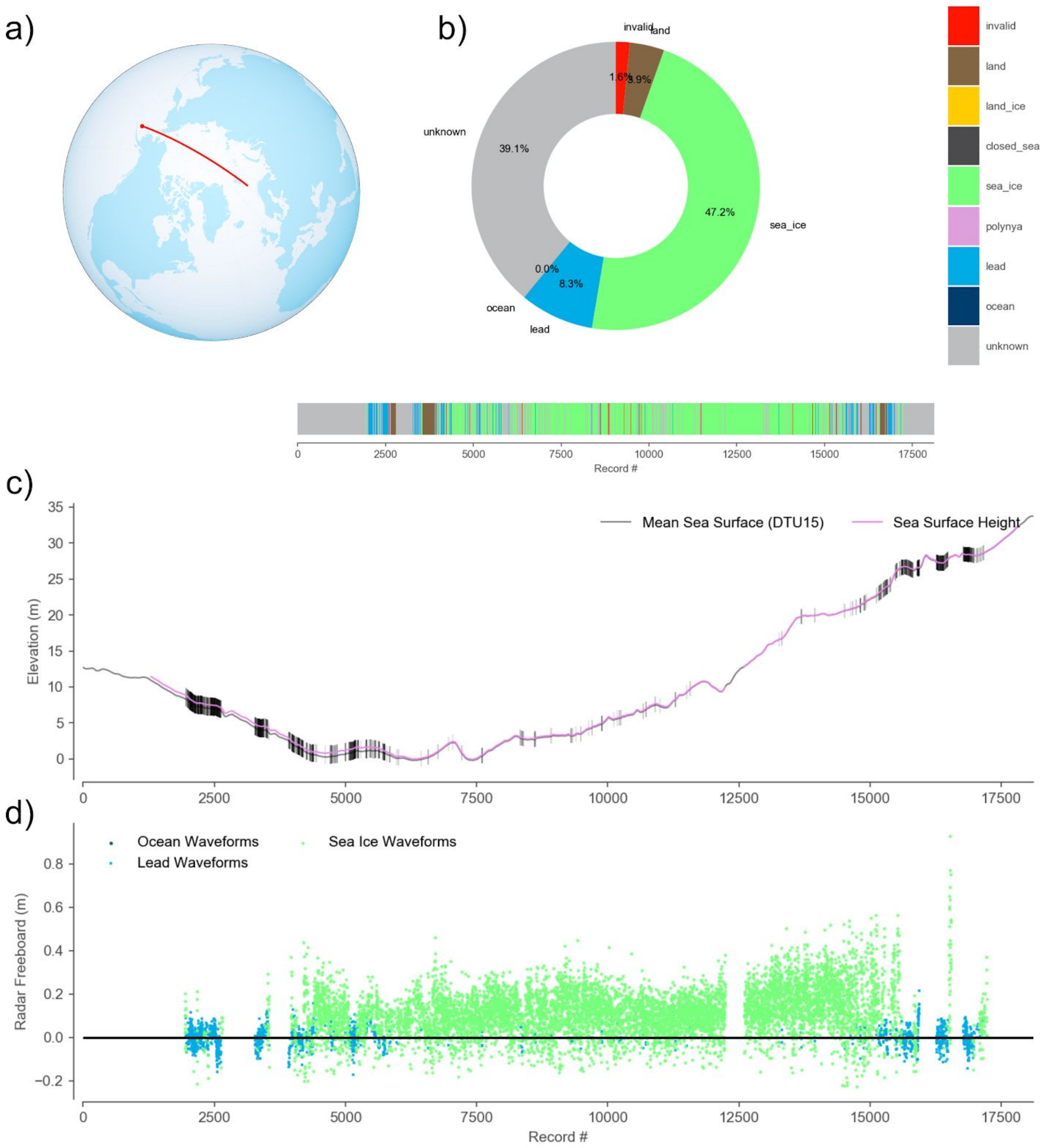

Figure 5-19: Example from along-track CryoSat-2 freeboard retrieval. a) Orbit location, b) surface type classification with classes unknown, lead and sea ice with percentage and geographical location along track c) Lead detections, mean sea surface height and sea surface height anomaly d) unfiltered radar freeboard

5.4.1 Sea-Surface Height Uncertainty

The uncertainty of the sea surface height depends on the base SSH uncertainty and the distance to the closest sea surface height tie point. The values for base ssh uncertainty is assumed to be 2 cm to include effects such as leads covered with thin ice and the maximum uncertainty is assumed as 10 cm (example of the value range in Figure 5-18) based on investigations of the typical variation of the anomaly between the instantaneous sea surface height and mean sea surface along polar crossing orbits.

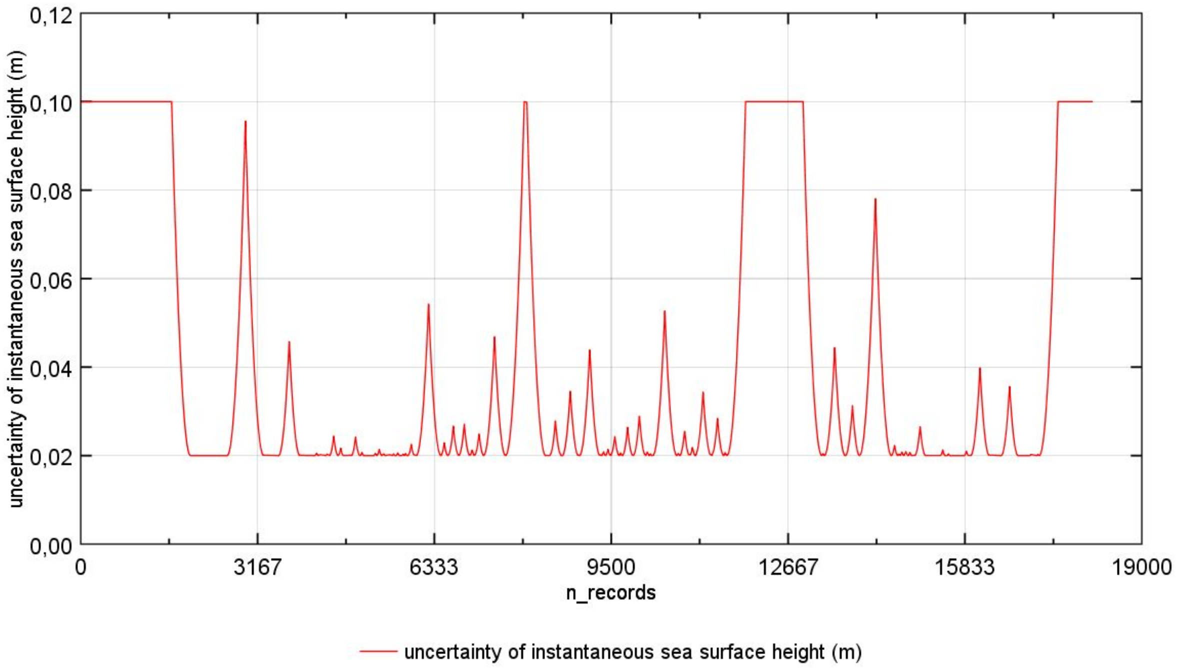

Figure 5-20: Example of Sea Surface Height Uncertainty

The sea surface height uncertainty is computed as

$$\sigma_{ssh} = \begin{cases} 0.02\,m + 0.1\,m \times \left(\frac{d_{tp}}{100\,km}\right)^2, \wedge d_{tp} < 100\,km \\ 0.1\,m, \wedge d_{tp} \geq 100\,km \end{cases}$$

With d_{tp} as the distance to the next sea surface height tie point.

5.4.2 Radar Freeboard Uncertainty

The radar freeboard uncertainty is computed by error propagation of the range or elevation uncertainty and the sea surface height uncertainty. For the simple case of radar freeboard being the difference between elevation and sea surface height, the radar freeboard uncertainty is given by:

$$\sigma_{rfrb} = \sqrt{\sigma_{elev}^2 + \sigma_{ssh}^2}$$

The elevation uncertainty σ_{elev} are fixed assumptions based on noise estimations for Envisat RA-2 und CryoSat-2 SIRAL sensors.

5.5 Snow on Sea Ice

In order to convert radar freeboard to sea-ice freeboard, a geometric correction has to be applied. For the Arctic, the W99 climatology used in SICCI Phase 2 has been replaced with a merged climatology created by AWI. This new snow product merges the monthly Warren snow climatology with daily snow depth from AMSR2 data, provided by the Institute for Environmental Physics of the University Bremen, over first-year sea ice, creating monthly snow depth fields.

For the merging of the two data sets, monthly composites of the AMSR2 snow depth fields are created to match the monthly resolution of the W99 climatology for the months from October to April. After that a Gaussian low pass filter with the size of 8 grid cells is applied on the AMSR2 snow depth composite, negative snow depths are removed and upper range limit is set to 60 cm. Then a regional weight factor w is created to ensure a smooth transition between the inner Arctic Basin domain and the area where AMSR2 is used. The merged snow depth (sd_{merged}) is computed as:

$$sd_{merged} = w \cdot sd_{W99} + (1 - w) \cdot sd_{AMSR2}$$

Figure 5-19 contains examples of the merging steps and Figure 5-20 for the regional weight factor.

Following the common practice to modify the W99 snow climatology by reducing the values by 50 % over first-year sea ice in the central Arctic (Tilling et al., 2018), the reduction is applied based on the ice type information for the particular orbit. This correction stems from Kurtz & Farrell 2011, that showed IceBridge measured snow thicknesses on FYI to be about 50% of the W99 estimates that are based on measurements made on MYI. Note that this scaling is applied only on the W99 snow, not on the AMSR2 snow depth. The scaled snow depth is:

$$c = (1 - f_{myi}) * c_{fyi} * w$$

$$sd = sd_{merged} - c \cdot sd_{merged}$$

Where c_{fyi} = 0.5 is the W99 scaling over first-year sea ice, c the total scaling factor including multiyear sea ice fraction f_{myi} and the weight factor.

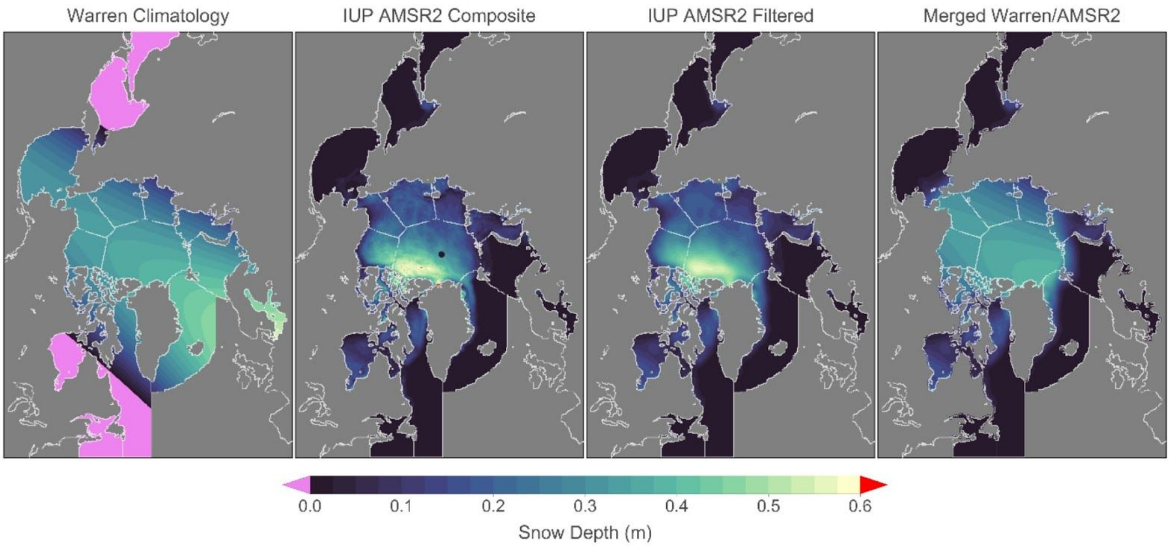

Figure 5-21: Steps for creating the monthly merged snow depth climatology. This example is for April, from left to right: 1) Warren snow depth climatology, 2) Monthly snow composite from daily AMSR2 data, 3) Low-pass filtered composite and 4) Merged Warren/AMSR2 with regional weight factor applied

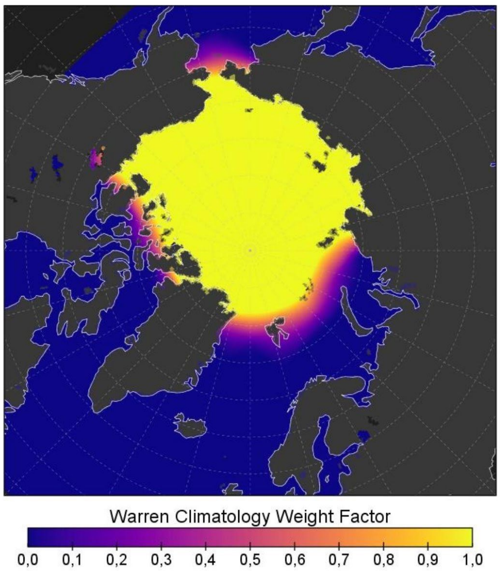

Figure 5-22: Regional weight factor for the W99 snow depth climatology

An example of the results with merged snow is in Figure 5-21. There are significantly less data gaps outside the central Arctic Basin, while retaining the W99 information on areas potentially covered with multiyear sea ice, areas where AMSR2 lacks sensitivity.

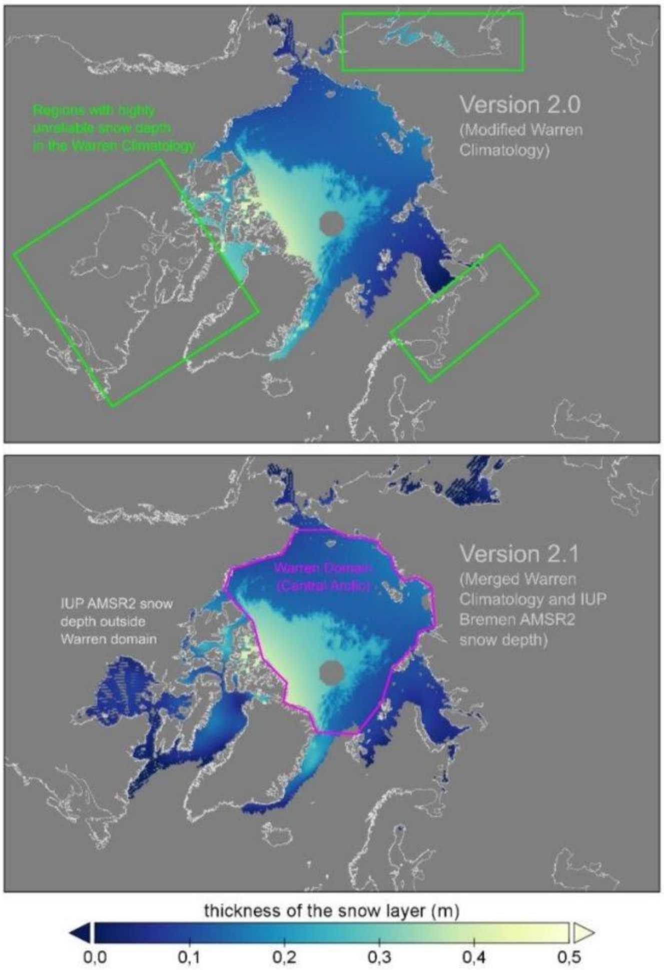

Figure 5-23: Performance example of sea ice thickness with the merged W99/AMSR2 snow product. Upper panel is the AWI CryoSat-2 v2.0 sea ice product with W99 snow and lower panel the sea ice thickness with merged W99/AMSR2 snow depth climatology. The improvements are most drastic in areas outside the domain (marked with green rectangles) of the W99 climatology (marked with purple polygon)

For Antarctic, with only a single ice type, a simpler approach is taken by applying the AMSR-E/2 snow-depth climatology provided by the ICDC. The climatology is based in averages for each calendar day of the daily data, available at the ICDC University Hamburg: (https://icdc.cen.uni-hamburg.de/en/esa-cci-sea-ice-ecv0.html).

5.5.1 Snow Depth Uncertainty

The Uncertainty of snow depth is taken from the input auxiliary data sets. In the case of the Arctic we use the information of inter-annual variability as an estimation for snow depth uncertainty. Since the snow depth (*sd*) is however modified by the MYI fraction, the uncertainty of the snow depth is also scaled on MYI fraction (f_{myi}) (50% of the original value for FYI and 100% for MYI respectively).

We also include an additional term that represents the effect MYI fraction uncertainty on the scaling assumption between FYI and MYI snow depth:

$$(Arctic)\sigma_{sd} = \underbrace{f_{myi} \times \sigma_{sd}^{W99}}_{Scaled\ W99\ Uncertainty} + \underbrace{sd \times (1 - f_{myi}) \times \sigma_{fmyi}}_{Scaling\ Uncertainty}$$

In the southern hemisphere the field `mediansnowdepth_filtered100_variability` of the snow depth climatology product is used as an uncertainty estimate.

5.5.2 Snow Density Uncertainty

In the Arctic the snow density uncertainty (σ_{ρ}^{s}) is provided by the Warren climatology as well. The difference in sea ice density between FYI and MYI is small, therefore the snow density and its uncertainty are assumed to be independent from the myi fraction.

In the Antarctic, we assume a fixed uncertainty of 20 kg/m3.

5.6 Sea-Ice Freeboard

The sea-ice freeboard is then calculated by adding this scaled snow-depth value times the reduction factor of the wave-propagation speed in snow compared to the vacuum speed of light. Valid sea ice freeboards are assumed to range from 0 to 2 meter, while the range is extended by the range noise (0.25 meter) for individual footprint. Thus orbit data outside the range of -0.25 m to 2.25 meter is filtered.

5.6.1 Sea-Ice Freeboard Uncertainty

In addition to the radar freeboard uncertainty, the sea ice freeboard uncertainty needs to take the component introduced by the snow wave speed correction into accounts. While the wave speed reduction is assumed to be reasonably well known, the additional uncertainty is controlled by snow depth uncertainty.

$$\sigma_{frb} = \sqrt{(sd \times \sigma_{sd})^2 + \sigma_{rfrb}^2}$$

5.7 Sea-Ice Thickness

5.7.1 Freeboard to Thickness

The final step in the processing is to convert sea-ice freeboard to sea-ice thickness. The ice floe may or may not be covered by snow, but field studies have shown that if the floe is indeed snow covered the radar reflection and hence height measurement relate to the snow ice interface. This however may not always be the case as was shown by the laser / radar altimeter study in Fram Strait during the RRDP exercise. This most certainly is not the case for areas of seasonal sea ice, such as the Baltic Sea, for most of the winter. Thus freeboard values should be understood as "altimeter freeboard" values. That is, for the cold central

Arctic they can be assumed to represent the ice freeboard, but for marginal areas the elevation measured is somewhere between the ice and snow freeboard. But since this effect cannot be parameterized with available EO observations, it is always assumed in the processing that the dominant reflector is the snow/ice interface.

Since the ice floe is in isostatic equilibrium, a simple calculation using freeboard and snow depth, and the densities of snow, sea ice and sea water, can be used to compute the thickness. Figure 5-22 illustrates this calculation. The final thickness is given by:

$$z_i = \frac{z_s\rho_s - f_b\rho_w}{\rho_w - \rho_i}$$

Where z_i is sea ice thickness, z_s snow depth, ρ_s snow density, f_b sea ice freeboard, ρ_w density of seawater and ρ_i density of sea ice.

In the Arctic, the snow depth and density are obtained from the Warren climatology (Warren et al., 1999). Since the snow depth measurements contributing to the Warren climatology originate exclusively from multi-year ice, the snow depth values are similarly scaled as for the snow geometric correction applied for the derivation of sea-ice freeboard from radar freeboard. As the Warren climatology is valid only in the central Arctic, we have to mask out measurements where it yields unreliable results (0.0 < snow depth < 0.6). This usually leads to masking of areas, for example Baffin Bay and the Baltic Sea in some months. We also follow the approach to scale the snow depth with the MYI fraction, leading to a 50% reduction of snow depth in FYI dominated regions. We only apply the MYI fraction scaling to snow depth and not density, as the latter is only marginally dependent on sea ice type.

For water density we use the fixed values of 1024 kg/m³. Direct measurements of sea ice density suggest that the density of multi-year ice is less than that of first-year ice. We therefore use a parameterization of the sea ice density that is scaled by the multi-year ice fraction between the density of multi-year ice (882 kg/m³) and first-year ice (916.7 kg/m³).

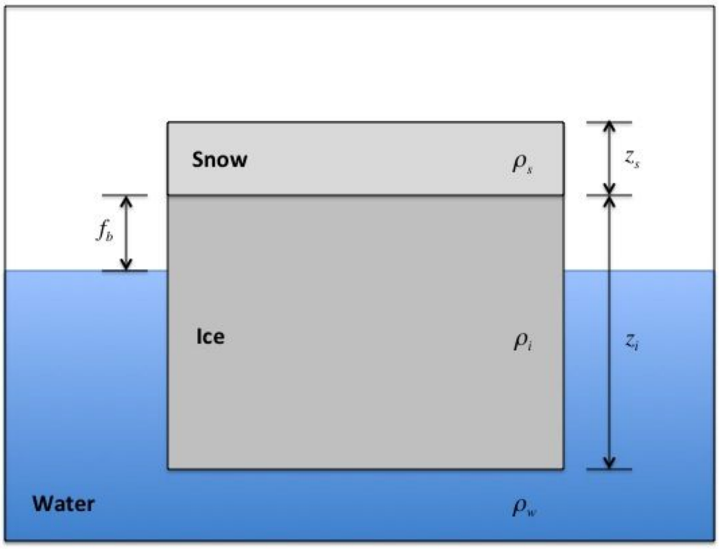

Figure 5-24: Computation of sea ice thickness

5.7.2 Sea Ice Density Uncertainty

Similar to snow depth, sea ice density (ρ_i) is a parameter obtained by scaling between the values for FYI and MYI using the myi fraction. To estimate the uncertainty (σ_ρ^i), we scale between the uncertainties of FYI (σ_ρ^{fyi}) and MYI density (σ_ρ^{myi}) and add a term for the scaling uncertainty.

$$\sigma_\rho^i = \underbrace{\sigma_\rho^{fyi} + f_{myi} \times \left(\sigma_\rho^{myi} - \sigma_\rho^{fyi}\right)}_{Uncertainty\ Scaling} + \underbrace{\sigma_{fmyi} \times \left(\sigma_\rho^{fyi} - \sigma_\rho^{myi}\right)}_{Scaling\ Uncertainty}$$

5.7.3 Sea Ice Thickness Uncertainty

The sea ice thickness uncertainty is computed as the error propagation of the input uncertainties.

$$\sigma_{sit} = \sqrt{\left(\frac{\rho_w}{\rho_w - \rho_i}\sigma_{frb}\right)^2 + \left(\frac{frb \cdot \rho_w + sd \cdot \rho_i}{\rho_w - \rho_i}\sigma_\rho^i\right)^2 + \left(\frac{\rho_s}{\rho_w - \rho_i}\sigma_{sd}\right)^2 + \left(\frac{sd}{\rho_w - \rho_i}\sigma_\rho^s\right)^2}$$

5.7.4 Sea Ice Type (MYI Fraction) Uncertainty

In the Arctic the myi fraction uncertainty (σ_{fmyi}) is taken directly from the MYI fraction product (field `my_sea_ice_area_fraction_sdev`)

No sea ice type product is available in the Antarctic and the general assumption is that all sea ice can be described as FYI. Nevertheless we assume a static uncertainty of 10% for the MYI fraction to account for sea ice type based uncertainties.

6 COLOCATION ON SPACE-TIME GRID (LEVEL-3 PROCESSOR)

Level-3 sea ice thickness is processed by mapping the orbit-based Level-2 data onto a spatiotemporal grid. The temporal and spatial dimensions are described in the following subsections.

6.1 Grid Temporal Coverage

The data will be processed for the winter season between October 1st and April 30th. Both weekly and monthly grids are available and their specifics are described in Table 6-1:

Table 6-1: Temporal definition for Level-3 products.

	Weekly	**Monthly**
Start of temporal coverage	Monday 00:00:00 UTC	First day of month 00:00:00 UTC
End of temporal coverage	Sunday 23:59:59.999 UTC	Last day of month 23:59:59.999 UTC

The Level-3 processing for these two temporal coverages differs only in the file naming, where the temporal level (weekly, monthly) is stated along with the start and end times of the temporal coverage.

6.2 Grid Spatial Definition

Data for both hemispheres will be gridded into the Equal-Area Scalable Earth Grid version 2 (EASE2-Grid) with 25km resolution. The projection is defined in Table 6-2 and grid extent and spacing in the Level-3 product are defined in Table 6-3.

Table 6-2: Projection definition for Level-3 products.

Property	**Value**
false_easting	0.0
false_northing	0.0
grid_mapping_name	lamber_azimuthal_equal_area
inverse_flattening	298.257223563
latitude_of_projection_origin	90.0
longitude_of_projection_origin	0.0
proj4_string	+proj=laea +lon_0=0 +datum=WGS84 +ellps=WGS84 +lat_0=90.0
semi_major_axis	6378137.0

Table 6-3: Grid extent and spacing for Level-3 products.

Property	**Value**
Grid Dimension	(432, 432)
Grid Spacing (km)	25.0
Grid Notation	Center Coordinates
Grid x extent in projection coordinates (km)	(-5387.5, 5387.5)

Grid y extent in projection coordinates (km)	(-5387.5, 5387.5)

6.3 Parameter Gridding

Level-3 processing will grid Level-2 intermediate (l2i) files. All the Level-2 data points within the specific timeframe are transformed into projection coordinates and assigned an index of a corresponding grid cell in the target grid. Each target grid cell will then possess a dedicated parameter stack that contains all the geophysical variables from Level-2 data that were associated with that specific cell. There is no filtering applied at this stage, except for radar freeboard, where freeboard values in leads need to be set as NaN in the Level-3 processor. The parameter stack of Level-2 data ($p_{i,L2}$) is used to compute the gridded parameter geophysical value p_{L3} as an arithmetic mean, ignoring non-numeric values:

$$p_{L3} = \frac{1}{n_{L2}} \cdot \sum_{i=0}^{n_{L2}} p_{i,L2} \qquad if\ p_{i,L2} \neq NaN$$

The geophysical parameters that will undergo gridding are:

1. radar freeboard
2. freeboard
3. sea ice thickness
4. sea surface anomaly
5. mean sea surface
6. snow depth
7. snow density
8. sea ice density
9. sea ice type
10. sea ice concentration

6.4 Level-3 Gridded Uncertainties

The Level-3 product contains the average uncertainties for freeboard/thickness respectively per grid cell to reflect that the biggest uncertainty components, e.g. snow depth, sea ice density, retracker biases, are not random uncertainties that would be reduced by averaging, examples in Figure 6-1. The uncertainties of the gridded radar freeboard, freeboard and sea ice thickness are therefore computed again with the error propagation functions, only that we use the weighted mean error for uncertainties of random variables (radar freeboard) and the average uncertainty from the orbit data for variables with systematic error components (snow depth, sea ice and snow density). This approach introduced in CCI+ results in a more realistic uncertainty magnitude compared to the SIT CRDP v2.0.

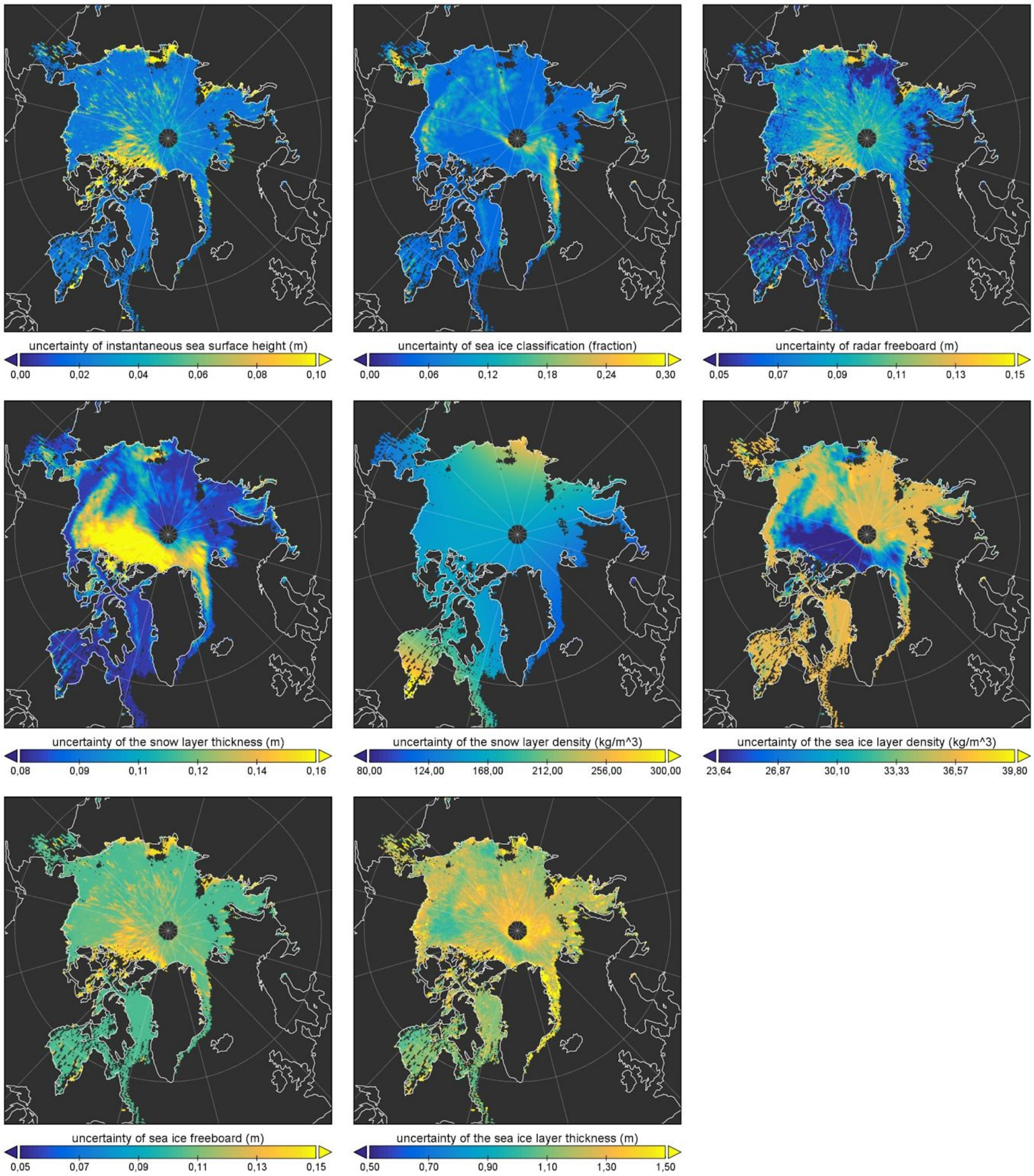

Figure 6-1: Gridded uncertainties (Example CryoSat-2 March 2015 Arctic data)

7 GAP INTERPOLATION (LEVEL-4 PROCESSOR)

This section is to be completed in the future versions of the document, but in general the level-4 data sets are created from lower level data and are interpolated in a way that they are gap-free.

Specifically, the Level-4 processor ingests sea-ice concentration data to determine where sea-ice thickness information needs to be available and computes an analysis of the available sea-ice thickness information from one or multiple platforms. One decision of the algorithm development will be if the source data for generating Level-4 products will be of Level-2 (trajectories) or Level-3 (space-time grids).

Level-4 sea-ice thickness information in the northern hemisphere will rely on interpolation over significant distances for the ERS-1/2 and Envisat platforms, as they provide only data up to 81.5 deg north. Appropriate auxiliary data sets guiding the interpolation over the pole hole will be identified, as well as the validity of such an approach.

8 SEA ICE VOLUME COMPUTATION

This section is to be completed in the future versions of the document.

For volume calculation, the individual sea ice thickness measurements are coupled with ice concentration values (C3S, Table 2-1). This is done on a gridded level product as area (of a grid cell) is needed. Volume is calculated only where ice concentration is above 15%, so an ice extent mask is applied to rule out areas outside the 15% concentration. Sea-ice volume is then the sum product of sea ice thickness, concentration and cell area of all grid cells.

9 REFERENCES

Armitage, T. W. K. and Davidson, M. Using the interferometric capabilities of the ESA CryoSat-2 mission to improve the accuracy of sea ice freeboard retrievals IEEE Trans. Geosci. Remote Sens., 52 (1), pp. 529-536, 2014.

Breiman, L. (2001) Random Forests. Machine Learning, 45, 5-32. http://dx.doi.org/10.1023/A:1010933404324

Cavalieri, D. J., T. Markus, and J. C. Comiso. 2014. AMSR-E/Aqua Daily L3 12.5 km Brightness Temperature, Sea Ice Concentration, & Snow Depth Polar Grids. Version 3. June 2002 – October 2011. Boulder, Colorado USA: NASA National Snow and Ice Data Center Distributed Active Archive Center. doi: http://dx.doi.org/10.5067/AMSR-E/AE_SI12.003.

Chelton, D. B., Ries, J. C., Haines, B. J., Fu, L.-L., and Callahan, P. S.: Satellite altimetry, International Geophysics, 69, 7–26, 2001.

Connor, L. N., Laxon, S. W., Ridout, A. L., Krabill, W. B., andMcAdoo, D. C.: Comparison of Envisat radar and airborne laser altimeter measurements over Arctic sea ice, Remote Sens. Environ., 113, 563–570, 2009.

Hartigan, J. A. and Wong, M. A.: Algorithm AS 136: A K-Means Clustering Algorithm, 28, 100–108, http://www.jstor.org/stable/2346830,1979.

Helm, V., Humbert, A., and Miller, H. (2014) Elevation and elevation change of Greenland and Antarctica derived from CryoSat-2, The Cryosphere, 8, 1539-1559, https://doi.org/10.5194/tc-8-1539-2014.

Kurtz N., Farrel SL.: Large-scale surveys of snow depth on Arctic sea ice from Operation IceBridge. Geophysical Research Letters, Vol. 38, L20505 2011. doi:10.1029/2011GL049216

Laxon, S. W., Peacock, N. R. & Smith, D. M. (2003) High interannual variability of sea ice thickness in the Arctic region. Nature, doi:10.1038/nature2050, 947-950.

MacQueen, J. (1967) Some methods for classification and analysis of multivariate observations. Proceedings of the Fifth Berkeley Symposium on Mathematical Statistics and Probability, Volume 1: Statistics, 281--297, University of California Press, Berkeley, Calif., https://projecteuclid.org/euclid.bsmsp/1200512992

Peacock, N. R. & Laxon, S. W. (2004) Sea surface height determination in the Arctic Ocean from ERS altimetry. Journal of Geophysical Research, Vol. 109, No. C7, C07001 10.1029/2001JC001026.

Ricker, R., Hendricks, S., Helm, V., Skourup, H., and Davidson, M. (2014) Sensitivity of CryoSat-2 Arctic sea-ice freeboard and thickness on radar-waveform interpretation, The Cryosphere, 8, 1607-1622, doi:10.5194/tc-8-1607-2014.

Tilling, R, Ridout, A., Shepherd, A.: Estimating Arctic sea ice thickness and volume using CryoSat-2 radar altimeter data. Advances in Space Research, Volume 62, Issue 6, 15 September 2018, Pages 1203-1225, doi: https://doi.org/10.1016/j.asr.2017.10.051

Warren, S. G., Rigor, I. G., Untersteiner, N., Radionov, V. F., Bryazgin, N. N., Aleksandrov, Y. I., and Colony, R. (1999) Snow depth on Arctic sea ice, J. Climate, 12, 1814–1829.